SWING STATE ESTIMATION AND CONTROL OF SERIES–CONNECTED SLUNG PAYLOADS IN ROTORCRAFT TRANSPORTATION

Elia Costantini[1], Emanuele L. de Angelis[*,2], Fabrizio Giulietti[3]

University of Bologna, Department of Industrial Engineering (DIN), CIRI Aerospace, Forlí, Italy 47121

Abstract

The use of rotorcraft with slung–load capabilities is increasingly relevant in applications ranging from aerial delivery to search–and–rescue. While existing research has extensively addressed single–payload systems, the present work investigates the estimation and control of swing dynamics in a rotorcraft transporting two serially–connected suspended payloads. A dynamic model of the system is derived via the Lagrangian approach, under the simplifying assumptions of point–mass vehicle and massless, rigid cables. The system is shown to be underactuated and its linearized dynamics about the hovering condition are used to formulate an estimation algorithm based on the Fading Gaussian Deterministic Filter (FGDF). This method uses only onboard accelerometer data to estimate swing angles and rates while minimizing the impact of model uncertainties and disturbances. The estimation is then embedded in a proportional feedback controller that stabilizes payload oscillations and maintains stability during dynamic events, such as load drop–off. The framework is validated through high–fidelity simulations of a heavy–lift octarotor. Results demonstrate improved swing suppression, energy efficiency, and operational continuity, confirming the approach's applicability to demanding aerial transport tasks and future urban delivery scenarios.

1. Introduction

Over the past few decades, towed–cable systems have been extensively researched for a wide range of rotorcraft applications, promoted by both civil and military interests that include: search–and–rescue, fire–fighting, transport of building material and emergency medical supplies, sensor deployment, vertical replenishment of seaborne vessels, and safe landmine detection (Ref. 1). As Unmanned Aerial Vehicle (UAV) research progressed, the evolution of highly automated air transport also began to generate interest. This resulted in the possibility of performing a wider range of transport tasks in risky and inaccessible zones as well as opening the path to future Urban Air Mobility and Delivery (UAMD) scenarios (Ref. 2).

The usage of towed–cable systems has different advantages with respect to solutions characterized by cargo compartments or manipulation devices, which allow for a quicker attachment/release of the load, but they increase the inertia moment of the system, thus making it slower and harder for agile maneuvers (Ref. 3). On the other hand, the suspension system allows greater flexibility in load distribution, enabling the same vehicle to carry larger or irregularly–shaped objects with improved balance. Additionally, the cable can passively dampen vibrations and shocks, which is beneficial especially for sensitive equipment such as cameras or scientific instruments. In the end, in applications like search–and–rescue or cargo delivery, the ability to lower and release payloads remotely reduces the need for precise landing and direct cooperation with recipients, enhancing operational efficiency and safety in challenging environments (Ref. 4). In this context, rotorcraft are known for their complex dynamic behavior, which becomes even more intricate when a cable–suspended payload is introduced, due to the additional degrees of freedom. Furthermore, if not properly controlled, the suspended payload can perturb vehicle's dynamics, potentially leading to system instability. This aspect increases the risk of collisions with obstacles, which could cause damage to both the payload and its surroundings (Ref. 5).

The problem of a single rotorcraft carrying a load has been addressed in the literature considering minimal load swing with the aim to support the secure transport of delicate or sensitive items, thus broadening the range of goods deliverable by air. Different control approaches are available, typically inspired by crane control problems. In Ref. 6, dynamic programming was employed to control swing–free trajectories, but performance limitations were experienced in open–loop configurations,

*Corresponding author
[1]Ph.D. Student, elia.costantini3@unibo.it
[2]Associate Professor, emanuele.deangelis4@unibo.it
[3]Professor, fabrizio.giulietti@unibo.it

leading researchers to explore closed–loop alternatives. In Ref. 7, a highly–nonlinear controller was derived to force the coupled slung–load system exhibiting a two–time–scale behavior, fast for the oscillation dynamics and slow for the trajectory–tracking task. The basic results of singular perturbation theory were evoked and a proof of almost–global asymptotic stability was provided. In Ref. 8, a control solution was presented to steer the aerial robot to a desired reference while limiting the sway of the payload. The stability of the equilibrium was proven through the application of a nested saturation control method for disturbance rejection. In Ref. 9, a Hamiltonian approach was adopted to suppress swing motion independently of the swing angle, provided that the assumed model accounted for a stiff, massless cable and a point–mass payload. In Ref. 10, both PD and sliding–mode control techniques were tested for a quadrotor and its slung–load system, demonstrating that sliding–mode control offers superior robustness to the disturbance effects of the cable–suspended load. Other approaches include an active–model–based control system supported by Kalman filtering (Ref. 11) and adaptive controllers for estimating unknown payload parameters (Ref. 12). In Ref. 13, a minimum–time trajectory planning method was presented that accounts for nonlinear dynamics and system constraints. Finally, input–shaping theory was also considered to reduce payload oscillations. In Ref. 14, input–shaping was combined with PID position control to improve trajectory–tracking and load stabilization, while enhanced control integrations for improved performance were respectively analyzed in Refs. 15 and 16 through sliding–mode and LQR methods.

To achieve anti–sway capabilities, accurately measuring load position is essential, with many solutions being inspired by bridge crane applications (Ref. 17). Common methods include motion capture systems, which provide precise estimates but require complex and costly installations (Refs. 18 and 19). While optical–based alternatives, such as visual detection (Ref. 20), could be considered, they often necessitate additional sensor devices, increasing take–off weight, power consumption, or making the system sensitive to environmental conditions (Ref. 21). Methods that do not rely on specialized camera systems generally use instruments fixed to the load. This is the case of high–accuracy GNSS devices (Ref. 22), which would be necessary for both the lifting vehicle and the load in outdoor environments. A novel technique for measuring sway angles using an inclinometer attached to the load was proposed in Ref. 23. In Ref. 24, the use of potentiometers was suggested to estimate the orientation of appendages in aerial manipulation tasks, with the ability to measure swing angles for suspended rigid links. Additionally, in Ref. 25, a method for estimating swing angles was developed using only an attached IMU module, with no external sensors. To this end, the authors derived an estimation algorithm for the disturbance force caused by the slung load using a disturbance observer. Since the direction of the tension force aligns with that of the wire, the swing angle could be directly estimated from force components. The limitations of the method were discussed, particularly the challenge of distinguishing load–induced forces from propulsive or other disturbance forces. In this respect, the authors proposed an alternative by using a load–cell mounted on the tether. In Ref. 26, two anti–sway trajectory generation methods were introduced based on linear models, providing dynamically feasible and optimal trajectories for the system. Notably, the authors mitigated aggressive motion and payload swing during transient responses by using a Kalman Filter (KF) to estimate payload state from onboard accelerometers and gyroscopes. Finally, in a recent study by one of the authors of the present paper (Ref. 27), a method to estimate swing angles in multirotor applications was presented, requiring no additional sensors other than the available onboard accelerometers. The approach combined sensor readings with dynamic model information using an FGDF filter. The method was validated through numerical simulations in the presence of model uncertainties. An improved version was later formulated in Ref. 28 according to the Extended Kalman Filter (EKF) formulation, showing enhanced estimation performance during agile maneuvers in the presence of unknown external disturbances, with both numerical and experimental validations.

In the present work, a rotorcraft transporting a set of two serially–connected suspended payloads is considered, with the aim to perform swing state estimation and control. First, the equations of motion of the coupled slung–load system are derived according to the Lagrangian approach. The obtained model is based on a set of simplifying assumptions that include the description of the lifting vehicle and the loads as a point–mass, while cables are assumed to be rigid and massless. An ad hoc parametrization of payload positions is proposed and the complete system is shown to be inherently underactuated. The model is linearized about the hovering condition with the payloads at rest and an observation algorithm is computed to allow the swing angles of the upper cable to be traced back to vehicles' accelerations over the local horizontal plane.

The estimation problem is solved recursively according to the FGDF approach, whose theoretical framework allows the identification of the optimal filter configuration that best dampens modeling errors with respect to measurement noise (Ref. 29). In such a way, the globally optimum filter (within its own class) is retrieved, with minimized estimation error. The estimated swing angles and rates are finally used in a novel proportional feedback control logic aiming at the stabilization of payloads oscillations. Controller structure is thus designed as an auxiliary contribution to available control loops specifically developed for rotorcraft guidance and navigation tasks.

The novelty of the approach, analyzed for the first time in the present work, is multifold: 1) the use of this method in parcel delivery, for example, potentially offers a multitude of benefits. Employing a multirotor system allows parcels to be transported swiftly and effectively, avoiding the limitations of traditional ground–based traffic. The capability to stabilize multiple serially–connected payloads permits the simultaneous delivery of more parcels in one flight, thus optimizing delivery routes and cutting operational costs; 2) the problem is addressed according to the FGDF method, which makes the estimation less prone to unknown external disturbances and/or non–modeled dynamics; 3) the architecture of the proposed controller is suitable for easy implementation in commercial–off–the–shelf control solutions of wide usage, such as the PX4 standard (Ref. 30); 4) in order to improve filter performance especially in windy conditions, a method is proposed to estimate and account the three components of aerodynamic disturbance force acting on the rotorcraft; 5) the method is broadly applicable and can be effectively adapted to various rotorcraft configurations, demonstrating significant improvements of flying qualities, operational safety, and energy efficiency; 6) the algorithm, developed here for the double-payload case, is well-suited for extension to scenarios involving a greater number of loads, thus enabling more flexible operations according to a possibly optimized delivery route. This outlines a prospective direction for future research, involving further model development, expanded observability analysis, and the resolution of technological challenges related to payload deployment.

The validity of the method and the performance of the controller are evaluated by numerical simulations in a realistic test case, where a heavy–lift octarotor system is detailed through the description of powerplant components and blade–element characterization of propellers. Sample maneuvers are proposed for a non–nominal scenario with viscoelastic cables in the presence of environmental disturbances, model uncertainties, and noisy sensor readings. A delivery mission is also analyzed where performance of the proposed estimation and control strategy is analyzed before and after dropping off the first (lower) payload, showing flexibility and continuity of operation. With the given problem's specific parametrization and the particular configuration of the controller, the approach is shown to be straightforward from the implementation standpoint, while providing the user with profound insights into the physical system.

2. System modeling

2.1. Reference frames

First, an Earth–fixed North–East–Down (NED) frame, denoted by $\mathcal{F}_E = \{O_E; \boldsymbol{x}_E, \boldsymbol{y}_E, \boldsymbol{z}_E\}$, is defined in accordance with Ref. 28 to be the inertial reference. Let P represent the center of gravity of the rotorcraft. Based on this, two sets of orthogonal, right–handed reference frames are introduced, that are rigidly attached to the rotorcraft:

- a Body–fixed frame: the rotorcraft is associated with a body–fixed frame $\mathcal{F}_B = \{P; \boldsymbol{x}_B, \boldsymbol{y}_B, \boldsymbol{z}_B\}$. The longitudinal axis $\boldsymbol{x}_B$ points outward through the nose in the plane of symmetry of the vehicle; the vertical axis $\boldsymbol{z}_B$ points downward along the fuselage/frame bottom and $\boldsymbol{y}_B$ completes the right–handed triad.

- a Structural frame: a structural reference frame $\mathcal{F}_S = \{O_S; \boldsymbol{x}_S, \boldsymbol{y}_S, \boldsymbol{z}_S\}$ is defined to locate the center of gravity and various vehicle components. Its axes are aligned with the body–fixed frame such that $\boldsymbol{x}_S = -\boldsymbol{x}_B$, $\boldsymbol{y}_S = \boldsymbol{y}_B$, and $\boldsymbol{z}_S = -\boldsymbol{z}_B$. The structural frame adopts a standard aircraft coordinate system: station lines (ST) are measured positively aft along the longitudinal axis, butt lines (BL) laterally to the right, and water lines (WL) vertically upward. Without loss of generality, a representative multirotor configuration is considered in which the origin O_S lies on the top surface of the frame and aligns vertically with the geometric center of the drone in the $\boldsymbol{x}_S$–$\boldsymbol{y}_S$ plane.

Transformation between the Earth frame $\mathcal{F}_E$ and the body–fixed frame $\mathcal{F}_B$ is achieved via the rotation matrix $\boldsymbol{T}_{BE}(\boldsymbol{\eta})$. Here, $\boldsymbol{\eta} = [\phi, \theta, \psi]^T$ encodes the attitude of the vehicle using the classical ZYX Tait–Bryan extrinsic rotation sequence, such that ϕ, θ, and ψ are commonly known as roll, pitch, and yaw angles (Ref. 31). Figure 1 provides a schematic of the rotorcraft and its associated reference frames.

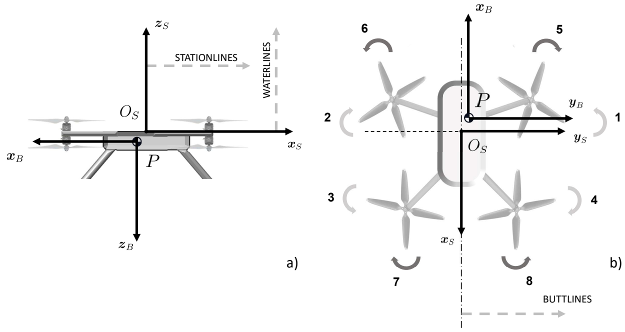

Figure 1: Multirotor body–fixed reference frames.

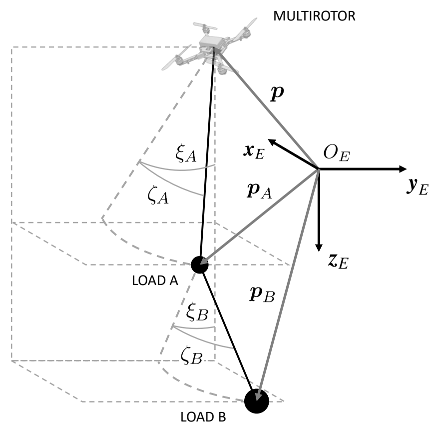

Figure 2: Definition of swing angles.

2.2. Equations of motion

Let $\boldsymbol{p} = [p_1,\, p_2,\, p_3]^T$ be the position of multirotor and $\boldsymbol{v} = [v_1,\, v_2,\, v_3]^T$ its velocity with respect to $\mathcal{F}_E$. Payload A, located in P_A, is assumed to be a point with mass m_A and is connected to the multirotor through a cable with constant length L_A. Similar considerations hold for payload B with mass m_B, located in P_B and connected to the upper payload by a cable with length L_B. Each cable is modeled as massless, under the assumption that its mass is negligible compared to the total mass of the system. It is further treated as a perfectly rigid element, implying no deformation under load and the ability to transmit both tensile and compressive forces, akin to an ideal rigid link, although, in practice, the transmission of compressive forces through cables is highly improbable. The dynamics of the vehicle as expressed in $\mathcal{F}_E$ (the subscript E will be dropped for simplicity) is described by:

$$\dot{\boldsymbol{p}} = \boldsymbol{v} \tag{1}$$

$$m\,\dot{\boldsymbol{v}} = \boldsymbol{f}_g + \boldsymbol{f}_A + \boldsymbol{f}_d + \boldsymbol{f}_c \tag{2}$$

where m is mass of the rotorcraft, $\boldsymbol{f}_g = [0,\, 0,\, m\,g]^T$ is gravity force vector, $\boldsymbol{f}_A$ is the force induced by the upper load on the rotorcraft through its cable, and $\boldsymbol{f}_d = [f_{d1},\, f_{d2},\, f_{d3}]^T$ is vehicle aerodynamic force, that accounts for the contributions of rotorcraft frame drag and rotor in–plane forces. The net thrust vector $\boldsymbol{f}_c = [f_{c1},\, f_{c1},\, f_{c1}]^T$, directed along $\boldsymbol{z}_B$, represents the only control input to Eq. (2).

The position of payload A with respect to the rotorcraft is parametrized by angles $-\pi/2 < \xi_A < \pi/2$ and $-\pi/2 < \zeta_A < \pi/2$, respectively obtained from load rotations about $\boldsymbol{x}_E$ and $\boldsymbol{y}_E$. The absolute position of payload A, identified by $\boldsymbol{p}_A = [p_{A1},\, p_{A2},\, p_{A3}]^T$, is thus expressed as a function of ξ_A, ζ_A, and $\boldsymbol{p}$ as

$$\begin{aligned}\boldsymbol{p}_A = \boldsymbol{p} + L_A \big[&\sin\zeta_A, \quad -\sin\xi_A\,\cos\zeta_A,\\ &\cos\xi_A\,\cos\zeta_A\big]^T\end{aligned} \tag{3}$$

Correspondingly, the position of payload B, given by $\boldsymbol{p}_B = [p_{B1},\, p_{B2},\, p_{B3}]^T$, is described as a function of $-\pi/2 < \xi_B < \pi/2$, $-\pi/2 < \zeta_B < \pi/2$, and $\boldsymbol{p}_A$ as

$$\begin{aligned}\boldsymbol{p}_B = \boldsymbol{p}_A + L_B \big[&\sin\zeta_B, \quad -\sin\xi_B\,\cos\zeta_B,\\ &\cos\xi_B\,\cos\zeta_B\big]^T\end{aligned} \tag{4}$$

Let $\boldsymbol{\lambda} = [\boldsymbol{p}^T,\, \xi_B,\, \zeta_B,\, \xi_A,\, \zeta_A]^T \in \mathbb{R}^7$ be a vector of generalized coordinates. The Lagrangian equation with respect to the generalized coordinate vector $\boldsymbol{\lambda}$ is (Ref. 27):

$$\frac{d}{dt}\left(\frac{\partial E}{\partial \dot{\boldsymbol{\lambda}}}\right) - \frac{\partial E}{\partial \boldsymbol{\lambda}} = \boldsymbol{\tau} \tag{5}$$

where $E = K - U$ is the Lagrangian function and $\boldsymbol{\tau} \in \mathbb{R}^7$ is the vector of generalized forces. In the present framework, K is system kinetic energy, given by

$$K = \frac{1}{2} m\,\dot{\boldsymbol{p}}^T \dot{\boldsymbol{p}} + \frac{1}{2} m_A\,\dot{\boldsymbol{p}}_A^T \dot{\boldsymbol{p}}_A + \frac{1}{2} m_B\,\dot{\boldsymbol{p}}_B^T \dot{\boldsymbol{p}}_B \tag{6}$$

where $\dot{\boldsymbol{p}}_A$ and $\dot{\boldsymbol{p}}_B$ denote load velocities as obtained from Eqs. (3) and (4), respectively. It is:

$$\begin{aligned}\dot{\boldsymbol{p}}_A = \dot{\boldsymbol{p}} + L_A \big[&\dot{\zeta}_A\, c\zeta_A, \quad -\dot{\xi}_A\, c\xi_A\, c\zeta_A + \dot{\zeta}_A\, s\xi_A\, s\zeta_A,\\ &-\dot{\xi}_A\, s\xi_A\, c\zeta_A - \dot{\zeta}_A\, c\xi_A\, s\zeta_A\big]^T\end{aligned} \tag{7}$$

and

$$\begin{aligned}\dot{\boldsymbol{p}}_B = \dot{\boldsymbol{p}}_A + L_B \big[&\dot{\zeta}_B\, c\zeta_B, \quad -\dot{\xi}_B\, c\xi_B\, c\zeta_B +\\ &+ \dot{\zeta}_B\, s\xi_B\, s\zeta_B,\\ &-\dot{\xi}_B\, s\xi_B\, c\zeta_B - \dot{\zeta}_B\, c\xi_B\, s\zeta_B\big]^T\end{aligned} \tag{8}$$

where $s(\cdot) = \sin(\cdot)$ and $c(\cdot) = \cos(\cdot)$. Potential energy U is related to the vertical displacement of the multirotor and the suspended loads, namely:

$$U = -m\, g\, p_3 - m_A\, g\, p_{A3} - m_B\, g\, p_{B3} \tag{9}$$

Given the energy contributions in Eqs. (6) and (9) and taking into account the state of the loads as described by Eqs. (3), (4), (7), and (8), the Lagrangian equation is manipulated into the system:

$$\dot{\boldsymbol{\lambda}} = \boldsymbol{\mu}, \qquad \boldsymbol{M}(\boldsymbol{\lambda})\, \dot{\boldsymbol{\mu}} + \boldsymbol{C}(\boldsymbol{\lambda}, \boldsymbol{\mu})\, \boldsymbol{\mu} + \boldsymbol{G}(\boldsymbol{\lambda}) = \boldsymbol{\tau} \tag{10}$$

where $\boldsymbol{\mu} = [\boldsymbol{v}^T, \dot{\xi}_B, \dot{\zeta}_B, \dot{\xi}_A, \dot{\zeta}_A]^T \in \mathbb{R}^7$. The generalized force vector $\boldsymbol{\tau}$ is made of an active control contribution, $\boldsymbol{\tau}_c = [\boldsymbol{f}_c^T, 0, 0, 0, 0]^T$, and a dissipative term, $\boldsymbol{\tau}_d = [\boldsymbol{f}_d^T, 0, 0, 0, 0]^T$, which accounts for the aerodynamic drag effects on the multirotor. The elements of $\boldsymbol{M} \in \mathbb{R}^{7\times 7}$ and $\boldsymbol{C} \in \mathbb{R}^{7\times 7}$ are reported in Appendix A, while $\boldsymbol{G} \in \mathbb{R}^7$ is defined as

$$\begin{aligned} \boldsymbol{G}(\boldsymbol{\lambda}) = \big[0, \quad 0, \quad & -(m_A + m_B), \\ & L_B\, m_B\, \sin\xi_B\, \cos\zeta_B, \\ & L_B\, m_B\, \cos\xi_B\, \sin\zeta_B, \\ & L_A\, m_A\, \sin\xi_A\, \cos\zeta_A, \\ & L_A\, m_A\, \cos\xi_A\, \sin\zeta_A\big]^T \end{aligned} \tag{11}$$

3. Swing state estimation

3.1. System linearization

The system in Eq. (10) is linearized about the equilibrium $(\bar{\boldsymbol{y}}, \bar{\boldsymbol{u}})$, where $\bar{\boldsymbol{y}} = [\bar{\boldsymbol{\lambda}}^T\, \bar{\boldsymbol{\mu}}^T]^T = [\bar{\boldsymbol{p}}^T\, \mathbf{0}_{1\times 11}]^T \in \mathbb{R}^{14}$ is representative of a hovering flight in $\boldsymbol{p} = \bar{\boldsymbol{p}}$ with the payloads at rest ($\bar{\xi}_A = \bar{\zeta}_A = \bar{\xi}_B = \bar{\zeta}_B = 0$, $\dot{\bar{\xi}}_A = \dot{\bar{\zeta}}_A = \dot{\bar{\xi}}_B = \dot{\bar{\zeta}}_B = 0$), provided the aerodynamic disturbance is a constant, $\bar{\boldsymbol{f}}_d$. The term $\bar{\boldsymbol{u}} \in \mathbb{R}^3$ represents the proper equilibrium force, provided $\bar{\boldsymbol{u}} = \bar{\boldsymbol{f}}_c + \bar{\boldsymbol{f}}_d$. The generalized equilibrium force is thus obtained as $\bar{\boldsymbol{\tau}} = \bar{\boldsymbol{\tau}}_c + \bar{\boldsymbol{\tau}}_d = \boldsymbol{G}(\bar{\lambda})$. Let $M = m + m_A + m_B$ be the total system mass. Taking into account the first 3 components in $\bar{\boldsymbol{\tau}}$, the proper equilibrium force is obtained as $\bar{\boldsymbol{u}} = [0, 0, -g\, M]^T$ while the control force generated by the rotorcraft is

$$\bar{\boldsymbol{f}}_c = \left[\bar{f}_{c_1}, \bar{f}_{c_2}, \bar{f}_{c_3}\right]^T = \bar{\boldsymbol{u}} - \bar{\boldsymbol{f}}_d \tag{12}$$

Let $\boldsymbol{y} = [\boldsymbol{\lambda}^T\, \boldsymbol{\mu}^T]^T \in \mathbb{R}^{14}$ and $\boldsymbol{u} \in \mathbb{R}^3$ be the state and input vectors respectively describing the dynamics in Eq. (10), linearized about $(\bar{\boldsymbol{y}}, \bar{\boldsymbol{u}})$. The standard state–space representation $\dot{\boldsymbol{y}} = \boldsymbol{A}\, \boldsymbol{y} + \boldsymbol{B}\, \boldsymbol{u}$ is derived where $\boldsymbol{A} \in \mathbb{R}^{14\times 14}$ is the state matrix,

$$\boldsymbol{A} = \left[\begin{array}{c|c|c} \mathbf{0}_{7\times 3} & \mathbf{0}_{7\times 4} & \boldsymbol{I}_7 \\ \hline \mathbf{0}_{7\times 3} & \begin{matrix} 0 & 0 & 0 & A_{8,7} \\ 0 & 0 & A_{9,6} & 0 \\ 0 & 0 & 0 & 0 \\ A_{11,4} & 0 & A_{11,6} & 0 \\ 0 & A_{12,5} & 0 & A_{12,7} \\ A_{13,4} & 0 & A_{13,6} & 0 \\ 0 & A_{14,5} & 0 & A_{14,7} \end{matrix} & \mathbf{0}_{7\times 7} \end{array}\right], \tag{13}$$

and $\boldsymbol{B} \in \mathbb{R}^{14\times 3}$ is the input matrix,

$$\boldsymbol{B} = \left[\begin{array}{ccc} \multicolumn{3}{c}{\mathbf{0}_{7\times 3}} \\ \hline B_{8,1} & 0 & 0 \\ 0 & B_{9,2} & 0 \\ 0 & 0 & B_{10,3} \\ 0 & 0 & 0 \\ 0 & 0 & 0 \\ 0 & B_{13,2} & 0 \\ B_{14,1} & 0 & 0 \end{array}\right] \tag{14}$$

In the present framework, $\boldsymbol{I}_p$ represents the unit matrix with dimension p, while $\mathbf{0}_{q\times r}$ is the null matrix with dimension $q\times r$. Non–null and non–unity terms in matrices $\boldsymbol{A}$ and $\boldsymbol{B}$ are, respectively:

$$A_{8,7} = -A_{9,6} = \frac{g\,(m_A + m_B)}{m} \tag{15}$$

$$A_{11,4} = A_{12,5} = -A_{11,6} = -A_{12,7} = -\frac{g\,(m_A + m_B)}{m_A\, L_B} \tag{16}$$

$$A_{13,4} = A_{14,5} = \frac{g\, m_B}{m_A\, L_A} \tag{17}$$

$$A_{13,6} = A_{14,7} = -\frac{g\,(m_A + m_B)(m + m_A)}{m\, m_A\, L_A} \tag{18}$$

$$B_{8,1} = B_{9,2} = \frac{1}{m} \tag{19}$$

$$B_{10,3} = \frac{1}{M} \tag{20}$$

$$B_{13,2} = -B_{14,1} = \frac{1}{m\, L_A} \tag{21}$$

3.2. Filter recursive equations

Let $\boldsymbol{x} = [x_1, x_2, x_3, x_4, x_5, x_6, x_7, x_8]^T = [\xi_B, \zeta_B, \xi_A, \zeta_A, \dot{\xi}_B, \dot{\zeta}_B, \dot{\xi}_A, \dot{\zeta}_A]^T \in \mathbb{R}^8$ be the state vector representing payload oscillation dynamics only. The linear time–invariant state–space model

$$\dot{\boldsymbol{x}} = \boldsymbol{A}_{pl}\, \boldsymbol{x} + \boldsymbol{B}_{pl}\, \boldsymbol{u} \tag{22}$$

is extracted from Eqs. (13) and (14), where

$$\boldsymbol{A}_{pl} = \left[\begin{array}{c|c} \mathbf{0}_{4\times 4} & \boldsymbol{I}_4 \\ \hline \begin{matrix} A_{11,4} & 0 & A_{11,6} & 0 \\ 0 & A_{12,5} & 0 & A_{12,7} \\ A_{13,4} & 0 & A_{13,6} & 0 \\ 0 & A_{14,5} & 0 & A_{14,7} \end{matrix} & \mathbf{0}_{4\times 4} \end{array}\right] \tag{23}$$

and

$$\text{(24)}\quad \boldsymbol{B}_{pl} = \left[\begin{array}{ccc} & \mathbf{0}_{6\times3} & \\ \hline 0 & B_{13,2} & 0 \\ B_{14,1} & 0 & 0 \end{array}\right]$$

The reduced–order dynamic model defined by Eqs. (22)–(24) is reformulated using difference equations where the true state vector $\boldsymbol{x}^{(k)}$ at time $t^{(k)}$ evolves according to $\boldsymbol{x}^{(k+1)} = \boldsymbol{\Phi}^{(k)}\boldsymbol{x}^{(k)} + \boldsymbol{\Psi}^{(k)}\boldsymbol{u}^{(k)}$. The state transition matrix used in the estimation algorithm is $\boldsymbol{\Phi}^{(k)} = \boldsymbol{\Phi} = \exp(\boldsymbol{A}_{pl}\,\Delta t)$, where $\Delta t = t^{(k+1)} - t^{(k)}$ is the sampling interval. The control–input model is determined as $\boldsymbol{\Psi}^{(k)} = \boldsymbol{\Psi} = \boldsymbol{A}_{pl}^{-1}(\boldsymbol{\Phi} - \boldsymbol{I}_8)\,\boldsymbol{B}_{pl}$. Eqs. (22)–(24) also provide:

$$\text{(25)}\quad a_1 = A_{8,7}\,\zeta_A + B_{8,1}\,u_1, \qquad a_2 = A_{9,6}\,\xi_A + B_{9,2}\,u_2$$

where $a_1 = \dot{v}_1$ and $a_2 = \dot{v}_2$ are vehicle acceleration components along $\boldsymbol{x}_E$ and $\boldsymbol{y}_E$, respectively. Eq. (25) infers the observability of oscillation angles ζ_A and ξ_A at time $t^{(k)}$, provided the concurrent input contributions u_1 and u_2 are known and acceleration components a_1 and a_2 are made available from sensors. A measurement model for the upper cable swing angles is thus derived where:

$$\text{(26)}\quad \xi_A^{(k)} = \frac{a_2^{(k)} - B_{9,2}\,u_2^{(k)}}{A_{9,6}}, \qquad \zeta_A^{(k)} = \frac{a_1^{(k)} - B_{8,1}\,u_1^{(k)}}{A_{8,7}}$$

The observation $\boldsymbol{z}^{(k)} = [\xi_A^{(k)},\,\zeta_A^{(k)}]^T$ with dimension $n = 2$ approximately tracks the considered dynamic process as in $\boldsymbol{z}^{(k)} = \boldsymbol{H}\,\boldsymbol{x}^{(k)}$, where

$$\text{(27)}\quad \boldsymbol{H} = \left[\ \mathbf{0}_{2\times2}\ \middle|\ \boldsymbol{I}_2\ \middle|\ \mathbf{0}_{2\times4}\ \right]$$

is a time–invariant observation matrix. It is finally assumed that measurements are corrupted by noise $\boldsymbol{\nu}^{(k)}$ with variance $\boldsymbol{R}$, that is $\boldsymbol{z}^{(k)} = \boldsymbol{H}\,\boldsymbol{x}^{(k)} + \boldsymbol{\nu}^{(k)}$.

Given the time series of data $\boldsymbol{z}^{(0)}, \boldsymbol{z}^{(1)}, \boldsymbol{z}^{(2)}, \ldots, \boldsymbol{z}^{(k)}$, the aim is to compute estimates to the state vector, namely $\tilde{\boldsymbol{x}}^{(0)}, \tilde{\boldsymbol{x}}^{(1)}, \tilde{\boldsymbol{x}}^{(2)}, \ldots, \tilde{\boldsymbol{x}}^{(k)}$, by taking into account the model in Eqs. (22)–(24). Such a problem is solved by the FGDF method as shown in Ref. 27, where the gain matrix is computed through the formal minimization of a cost function, with no other assumption (Ref. 29). Let $\boldsymbol{R}^\star$ be an assigned weighting matrix, with dimensions $n \times n$, and $\beta \in (0, 1)$ be the fading factor. By accounting $\boldsymbol{H}$, $\boldsymbol{\Phi}$, and $\boldsymbol{\Psi}$, the following recursive equations are considered:

1. Input:

   $$\text{(28)}\quad \boldsymbol{z}^{(k)},\ \tilde{\boldsymbol{x}}^{(k)-},\ \boldsymbol{E}^{(k)-}$$

2. Compute:

   $$\text{(29)}\quad \tilde{\boldsymbol{x}}^{(k)} = \tilde{\boldsymbol{x}}^{(k)-} + \boldsymbol{M}^{(k)}\left[\boldsymbol{z}^{(k)} - \boldsymbol{H}\tilde{\boldsymbol{x}}^{(k)-}\right]$$

   where

   - *standard formulation*

     $$\text{(30)}\quad \boldsymbol{M}^{(k)} = \boldsymbol{E}^{(k)-}\boldsymbol{H}^T\left[\boldsymbol{H}\boldsymbol{E}^{(k)-}\boldsymbol{H}^T + \boldsymbol{R}^\star\right]^{-1}$$

     $$\text{(31)}\quad \boldsymbol{E}^{(k)} = \left[\boldsymbol{I}_m - \boldsymbol{M}^{(k)}\boldsymbol{H}\right]\boldsymbol{E}^{(k)-}$$

   - *alternative formulation*

     $$\text{(32)}\quad {\boldsymbol{E}^{(k)}}^{-1} = \boldsymbol{H}^T\boldsymbol{R}^{\star-1}\boldsymbol{H} + \left[\boldsymbol{E}^{(k)-}\right]^{-1}$$

     $$\text{(33)}\quad \boldsymbol{M}^{(k)} = \boldsymbol{E}^{(k)}\boldsymbol{H}^T\boldsymbol{R}^{\star-1}$$

3. Project ahead:

   $$\text{(34)}\quad \tilde{\boldsymbol{x}}^{(k+1)-} = \boldsymbol{\Phi}\tilde{\boldsymbol{x}}^{(k)} + \boldsymbol{\Psi}\boldsymbol{u}^{(k)}$$

   $$\text{(35)}\quad \boldsymbol{E}^{(k+1)-} = \frac{\boldsymbol{\Phi}\boldsymbol{E}^{(k)}\boldsymbol{\Phi}^T}{\beta}$$

In this framework, quantities marked with a minus superscript denote the predicted (a priori) filter estimates, derived from the model–based forward projection in Eqs. (34) and (35). The updated (a posteriori) estimates, which incorporate the current measurement and are adjusted using the gain matrix $\boldsymbol{M}^{(k)}$, are computed using Eqs. (29) and (31) or, alternatively, via Eq. (32).

Remark 1 The global optimization of the FGDF is addressed as shown in Ref. 29, leveraging the specific characteristics of the estimation strategy. The optimization process involves two main steps: tuning the fading parameter and scaling the noise covariance matrix. To achieve this, a bank of filters is considered, each receiving the same input data $\boldsymbol{z}^{(k)}$ but differing in the value of the fading factor β. For each filter configuration, two performance metrics are evaluated as functions of β: a tuning statistic ${\chi^{(k)}}^2(\beta)$ and a scaling statistic ${\xi^{(k)}}^2(\beta)$, both defined in Ref. 29. The tuning statistic is then averaged over a selected time window, yielding $\overline{\chi^2}(\beta)$. The optimal value β_T is identified as the one minimizing this averaged tuning statistic:

$$\text{(36)}\quad \overline{\chi^2}(\beta_T) = \min_{\beta\in(0,\,1)}\left[\overline{\chi^2}(\beta)\right]$$

This optimal fading factor β_T is interpreted as providing the best overall balance between model prediction and measurement correction, minimizing estimation error by optimally fading past residuals. Once β_T is determined, the corresponding average of the scaling statistic, $\overline{\xi^2}(\beta_T)$, is used to compute an effective gain factor for scaling the nominal covariance $\boldsymbol{R}^\star$ to an estimate of the actual measurement noise covariance $\boldsymbol{R}$:

$$\text{(37)}\quad \tilde{\boldsymbol{R}} = \overline{\xi^2}(\beta_T)\,\boldsymbol{R}^\star$$

Consequently, the true error covariance matrix $\boldsymbol{P}^{(k)}$ can be approximated from the filter–computed covariance $\boldsymbol{E}^{(k)}$ as:

(38) $$\tilde{\boldsymbol{P}}^{(k)}(\beta_T) = \overline{\xi^2}(\beta_T)\,\boldsymbol{E}^{(k)}(\beta_T)$$

In this tuned and scaled configuration, where the adjusted nominal covariance aligns with the true estimation error, the approach yields a minimum in the trace of $\boldsymbol{P}^{(k)}$, thereby demonstrating the capability of the method to achieve globally optimal filter performance.

4. Results

This section details the configuration of the proposed estimation method to ensure optimal performance, followed by its validation within a numerical simulation environment. Thereafter, a representative delivery mission is examined to assess the effectiveness of payload control strategies derived from the estimated swing dynamics.

4.1. Simulation setup

Simulations are performed in Matlab® with a 4th–order Runge–Kutta solver frequency of 500 Hz (Ref. 32). Air parameters are calculated from the International Standard Atmosphere (ISA) model as a function of altitude (Ref. 33). The octarotor is modeled as a rigid body according to the blade–element approach and nomenclature introduced in Ref. 28, where vehicle data are reported in detail. Table 1 resumes some relevant parameters of the coupled slung–load system. Let $\boldsymbol{c}_A = \boldsymbol{p}_A - \boldsymbol{p}_H$ be the vector describing the orientation and length of cable A, provided $\boldsymbol{p}_H$ indicates the position of the hook point as expressed in $\mathcal{F}_E$. Provided STA_H, BL_H, and WL_H are, respectively, the stationline, buttline, and waterline of the hook point H, it is $\boldsymbol{p}_H = \boldsymbol{p} + \boldsymbol{T}_{BE}^T\,[STA_P - STA_H,\, BL_H - BL_P,\, WL_P - WL_H]^T$. The force $\boldsymbol{f}_A$ in Eq. (2) is calculated as $\boldsymbol{f}_A = \left(K_A\,\Delta L_A + C_A\,\Delta\dot{L}_A\right)\hat{\boldsymbol{c}}_A$, where $\hat{\boldsymbol{c}}_A = \boldsymbol{c}_A/\left\|\boldsymbol{c}_A\right\|$, K_A is the elastic constant, and $\Delta L_A = \|\boldsymbol{c}_A\| - L_A$ and $\Delta\dot{L}_A$ are, respectively, the elastic deformation and its time derivative. Similarly, the force exerted by load B on load A is calculated as $\boldsymbol{f}_B = \left(K_B\,\Delta L_B + C_B\,\Delta\dot{L}_B\right)\hat{\boldsymbol{c}}_B$, where $\boldsymbol{c}_B = \boldsymbol{p}_B - \boldsymbol{p}_A$ and K_B is the elastic constant considered for the deformation $\Delta L_B = \|\boldsymbol{c}_B\| - L_B$. With respect to the classical Hookes' model in Ref. 28, cable internal damping is accounted by coefficients $C_A = C_B = 250$ N m^{-1} s, assigned to be equal. Both payloads are affected by aerodynamic drag, provided $A_A = \pi\,R_A^2$ and $A_B = \pi\,R_B^2$ are the reference areas of equivalent spheres with radii $R_A = 0.5$ m and $R_B = 0.35$ m and drag coefficients $C_{dA} = C_{dB} = 0.5$.

The dynamics of each electric propulsion unit, comprising an Electronic Speed Controller (ESC) and a brushless motor, are represented by a first–order transfer function with time constant $\tau_{em} = 0.05$ s, capturing both electrical and mechanical non–idealities. This transfer function maps the commanded rotor angular rate to the actual rate delivered by the motor shaft.

Table 1: System parameters.

Parameter	**Symbol**	**Value**	**Units**
Multirotor			
Mass	m	70	kg
Center of gravity position	$STA_P = BL_P$	0	m
	WL_P	-0.15	m
Frame drag areas	$A_1 = A_2$	0.22	m^2
	A_3	1.03	m^2
Center of pressure position	$STA_{CP} = BL_{CP}$	0	m
	WL_{CP}	-0.125	m
Hook point position	$STA_H = BL_H$	0	m
	WL_H	-0.2	m
Propeller			
Number of blades	n_b	2	-
Radius	R	0.5	m
Mean aerodynamic chord	$\bar{c}$	0.086	m
Load A			
Mass	m_A	60	kg
Reference area	A_A	0.785	m^2
Drag coefficient (sphere)	C_{dA}	0.5	-
Cable A			
Nominal length	L_A	10	m
Hooke's constant	K_A	136 424	N m^{-1}
Damping coefficient	C_A	250	N m^{-1} s
Load B			
Mass	m_B	40	kg
Reference area	A_B	0.385	m^2
Drag coefficient (sphere)	C_{dB}	0.5	-
Cable B			
Nominal length	L_B	5	m
Hooke's constant	K_B	272 847	N m^{-1}
Damping coefficient	C_B	250	N m^{-1} s

Non–ideal sensing behavior is considered where noise, bias, and sensor positioning errors are introduced and described from a numerical standpoint. Onboard computer is located at $STA_{PIX} = BL_{PIX} = 0$ m and $WL_{PIX} = -0.1$ m, with axes aligned with $\mathcal{F}_B$–axes. To simulate the effects of sensor noise, zero–mean Gaussian white noise is added to each Euler angle and angular velocity measurement, with standard deviations $\sigma_\alpha = 0.018$ deg and $\sigma_\omega = 0.095$ deg/s, respectively. The body–fixed accelerometer readings are obtained by adding white Gaussian noise with $\sigma_{acc} = 0.015$ m/s^2 and constant bias $\boldsymbol{a}_{bias} = [0.015,\,-0.01,\,0.002]^T$ m/s^2 to the simulated values. Error is also considered for vehicle position and velocity expressed in $\mathcal{F}_E$, provided standard deviations $\sigma_p|_{xy} = 0.074$ m and $\sigma_v|_{xy} = 0.009$ m/s affect the motion over the local–horizontal plane, while $\sigma_p|_z = 0.034$ m and $\sigma_v|_z = 0.005$ m/s characterize the vertical component. The onboard computer operates at a frequency of 100 Hz (sample time $\delta_t = 0.01$ s).

4.2. Control system

Without loss of generality, a cascaded controller based on PX4 architecture and notation (Ref. 30) is adopted to stabilize the octarotor across various flight modes, ranging from high–level position control to low–level attitude regulation (see Figure 3). While a comprehensive analysis of the PX4 control framework lies beyond the scope of this paper, it is assumed that the vehicle is stabilized in accordance with specified flying qualities through appropriate tuning of the control parameters.

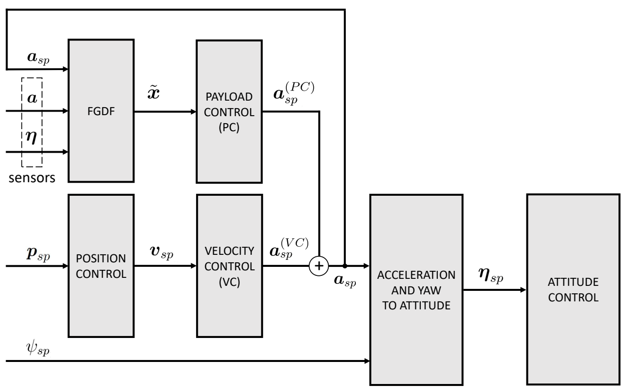

Figure 3: Multirotor control scheme based on PX4 autopilot architecture (Ref. 30).

Desired acceleration $\boldsymbol{a}_{sp} = [a_{sp_1},\, a_{sp_2},\, a_{sp_3}]^T$ is designed as

$$(39)\quad \boldsymbol{a}_{sp_i} = \boldsymbol{a}_{sp}^{(VC)} + \boldsymbol{a}_{sp}^{(PC)}$$

where $\boldsymbol{a}_{sp}^{(VC)}$ allows trajectory–following through the tracking of setpoint speed $\boldsymbol{v}_{sp}$ (Velocity Control) while $\boldsymbol{a}_{sp}^{(PC)}$ implements Payload Control strategies. Let $k_p > 0$ and $k_v > 0$ be control gains. The following controller is proposed:

$$(40)\quad \begin{aligned} \boldsymbol{a}_{sp}^{(PC)} &= \mathrm{diag}(1,\,1,\,0)\,\big[k_p\,(\boldsymbol{p}_C - \boldsymbol{p}_H) + \\ &\quad + k_v\,(\boldsymbol{v}_C - \boldsymbol{v}_H)\big] \end{aligned}$$

where $\boldsymbol{p}_C$ is the absolute position of the center of gravity C of the payload system, obtained as

$$(41)\quad \boldsymbol{p}_C = \frac{m_A\,\boldsymbol{p}_A + m_B\,\boldsymbol{p}_B}{m_A + m_B}$$

while $\boldsymbol{v}_C$ is the corresponding speed, namely

$$(42)\quad \boldsymbol{v}_C = \frac{m_A\,\boldsymbol{v}_A + m_B\,\boldsymbol{v}_B}{m_A + m_B}$$

Assuming $\boldsymbol{p}_H \approx \boldsymbol{p}$ and considering Eq. (41), one has:

$$(43)\quad \boldsymbol{p}_C - \boldsymbol{p}_H \approx \boldsymbol{p}_C - \boldsymbol{p} \approx \frac{m_A\,(\boldsymbol{p}_A - \boldsymbol{p}) + m_B\,(\boldsymbol{p}_B - \boldsymbol{p})}{m_A + m_B}$$

Taking into account Eqs. (3) and (4), one derives

$$(44)\quad \begin{aligned} \boldsymbol{p}_C - \boldsymbol{p}_H \approx\ & L_A\,\big[\sin\zeta_A,\quad -\sin\xi_A\,\cos\zeta_A, \\ & \cos\xi_A\,\cos\zeta_A\big]^T \\ & + \frac{m_B\,L_B}{m_A + m_B}\,\big[\sin\zeta_B,\quad -\sin\xi_B\,\cos\zeta_B, \\ & \cos\xi_B\,\cos\zeta_B\big]^T \end{aligned}$$

In the same way, by considering Eqs. (7) and (8), it follows:

$$(45)\quad \begin{aligned} \boldsymbol{v}_C - \boldsymbol{v}_H \approx\ & L_A\,\big[\dot\zeta_A\,c\zeta_A, \\ & -\dot\xi_A\,c\xi_A\,c\zeta_A + \dot\zeta_A\,s\xi_A\,s\zeta_A, \\ & -\dot\xi_A\,s\xi_A\,c\zeta_A - \dot\zeta_A\,c\xi_A\,s\zeta_A\big]^T \\ & + \frac{m_B\,L_B}{m_A + m_B}\,\big[\dot\zeta_B\,c\zeta_B, \\ & -\dot\xi_B\,c\xi_B\,c\zeta_B + \dot\zeta_B\,s\xi_B\,s\zeta_B, \\ & -\dot\xi_B\,s\xi_B\,c\zeta_B - \dot\zeta_B\,c\xi_B\,s\zeta_B\big]^T \end{aligned}$$

In the present framework, swing angles and rates are obtained from the proposed estimation algorithm while the selected values of control gains in Eq. (40) are, respectively, $k_p = 1.2$ 1/s^2 and $k_v = 0.4$ 1/s.

Remark 2 The controller described in Eq. (40) relies on the heuristic feedback of the relative position of payload system's center of gravity with respect to the hook point. Such an approach stems from the one adopted in Ref. 28, where a single payload was considered, being representative of a more general case. Provided $m_B = 0$ kg, which situation occurs after dropping off the first (lower) payload and cable, the closed–loop system reverts to the single payload scenario and $\boldsymbol{P}_C \equiv \boldsymbol{P}_A$. In such a case, the relative position and velocity of the remaining load is used as a feedback term proportional to the swing angles and rates as in Ref. 28, thus inferring flexibility and continuity in usage of the same control law over the entire mission.

In accordance with the control architecture of PX4 autopilot, a systematic and effective approach is employed to reconstruct the input force, defined as $\boldsymbol{u} = \boldsymbol{f}_c + \boldsymbol{f}_d$. Under the assumption of ideal electric motor behavior, the thrust magnitude is approximated as $\tilde{T} = (m + m_A + m_B)\,\|\boldsymbol{a}_{sp}\|$. Taking into account the vehicle's attitude dynamics, the control force expressed in the inertial frame $\mathcal{F}_E$ is estimated as $\tilde{\boldsymbol{f}}_c = \boldsymbol{T}_{BE}^T(\tilde{\boldsymbol{\eta}})\,[0,\,0,\,-\tilde{T}]^T$. With regard to the characterization of external disturbances, it is noted that the velocity control module shown in Fig. 3 is implemented as a conventional PID controller (Ref. 30). The latter converts the velocity–tracking error into a desired acceleration, expressed as $\boldsymbol{a}_{sp}^{(VC)} = \boldsymbol{a}_{sp}^{(VC)}\Big|_P + \boldsymbol{a}_{sp}^{(VC)}\Big|_I + \boldsymbol{a}_{sp}^{(VC)}\Big|_D$, where the subscripts P, I, and D respectively denote the proportional, integral, and derivative contributions. By considering quasi–steady external disturbances and taking advantage of the integral component's well–known ability to reject such disturbances (Ref. 34), the disturbance force is conservatively modeled as $\tilde{\boldsymbol{f}}_d = -(m + m_A + m_B)\ \boldsymbol{a}_{sp}^{(VC)}\Big|_I$. Accordingly, the estimated total input force is given by $\tilde{\boldsymbol{u}} = \boldsymbol{T}_{BE}^T(\tilde{\boldsymbol{\eta}})\,[0,\,0,\,-\tilde{T}]^T - (m + m_A + m_B)\ \boldsymbol{a}_{sp}^{(VC)}\Big|_I$, where the latter contribution accounts for the aerodynamic drag force exerted on the whole system, payloads included.

4.3. Tuning and scaling procedures

Consider system parameters in Table 1. Equations (23) and (24) respectively provide:

$$(46)\quad \boldsymbol{A}_{pl} = \left[\begin{array}{cccc|c} \multicolumn{4}{c|}{\mathbf{0}_{4\times4}} & \boldsymbol{I}_4 \\ \hline -3.2689 & 0 & 3.2689 & 0 & \\ 0 & -3.2689 & 0 & 3.2689 & \mathbf{0}_{4\times4} \\ 0.6538 & 0 & -3.0354 & 0 & \\ 0 & 0.6538 & 0 & -3.0354 & \end{array}\right]$$

and

$$(47)\quad \boldsymbol{B}_{pl} = \left[\begin{array}{ccc} \multicolumn{3}{c}{\mathbf{0}_{6\times3}} \\ \hline 0 & 0.0014 & 0 \\ -0.0014 & 0 & 0 \end{array}\right]$$

The state–transition matrix is computed by Matlab® matrix exponential function $expm(\cdot)$ according to the method in Ref. 35:

$$(48)\quad \boldsymbol{\Phi} = \begin{bmatrix} 0.9998 & 0 & 0.0002 & 0 & 0.0100 & 0 & 0 & 0 \\ 0 & 0.9998 & 0 & 0.0002 & 0 & 0.0100 & 0 & 0 \\ 0 & 0 & 0.9998 & 0 & 0 & 0 & 0.0100 & 0 \\ 0 & 0 & 0 & 0.9998 & 0 & 0 & 0 & 0.0100 \\ -0.0327 & 0 & 0.0327 & 0 & 0.9998 & 0 & 0.0002 & 0 \\ 0 & -0.0327 & 0 & 0.0327 & 0 & 0.9998 & 0 & 0.0002 \\ 0.0065 & 0 & -0.0304 & 0 & 0 & 0 & 0.9998 & 0 \\ 0 & 0.0065 & 0 & -0.0304 & 0 & 0 & 0 & 0.9998 \end{bmatrix}$$

The control–input function is

$$(49)\quad \boldsymbol{\Psi} = \begin{bmatrix} 0 & 0 & 0 \\ -0 & 0 & 0 \\ 0 & 0.0007 & 0 \\ -0.0007 & 0 & 0 \\ 0 & 0 & 0 \\ -0 & 0 & 0 \\ 0 & 0.1428 & 0 \\ -0.1428 & 0 & 0 \end{bmatrix} \cdot 10^{-4}$$

according to the formulation reported in Section 3.

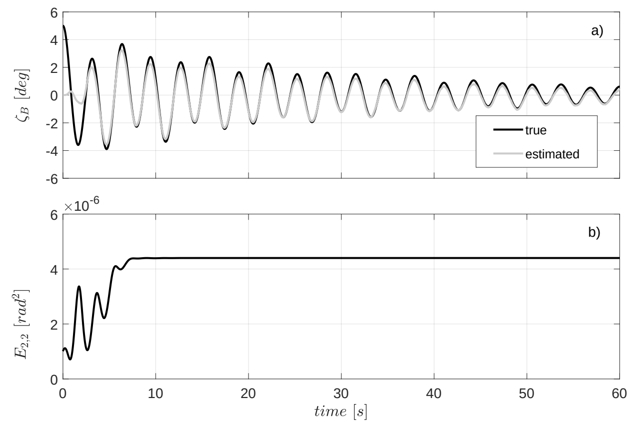

Figure 4: a) Comparison between the true and the estimated ζ_B angle. b) Estimation convergence for the nominal covariance component $E_{2,2}$.

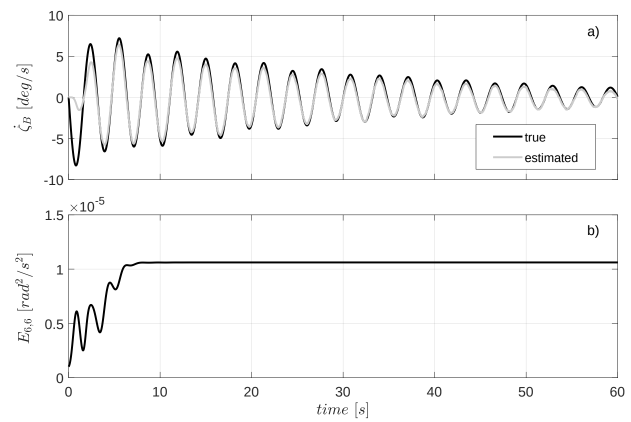

Figure 5: a) Comparison between the true and the estimated $\dot{\zeta}_B$ angular rate. b) Estimation convergence for the nominal covariance component $E_{6,6}$.

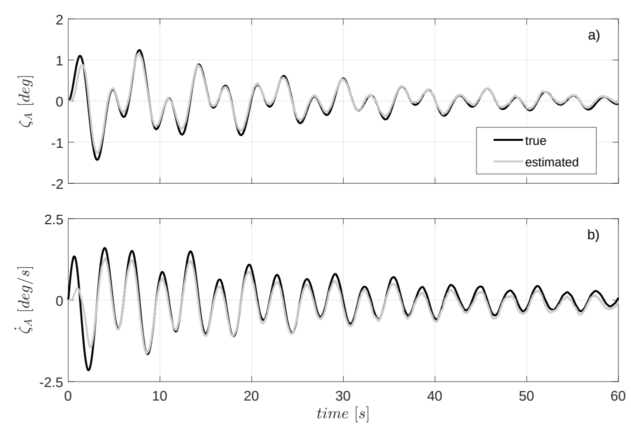

Figure 6: a) Comparison between the true and the estimated values of a) ζ_A angle and b) $\dot{\zeta}_A$ angular rate.

A representative maneuver is designed to facilitate filter optimization by tuning the fading factor. The filter's initial state estimate is set to $\tilde{\boldsymbol{x}}^{(0)-} = \boldsymbol{0}_{8\times1}$ and the nominal covariance matrix is initialized as $\boldsymbol{E}^{(0)-} = \mathrm{diag}(10^{-6}, 10^{-6}, 10^{-8}, 10^{-8}, 10^{-6}, 10^{-6}, 10^{-7}, 10^{-7})$. Acceleration information are converted to measured oscillation angles through Eq. (26). In this case, the covariance σ^2_{acc} must be scaled by the factor $1/A_{8,7} = |1/A_{9,6}| = m/g/(m_A+m_B)$, such that one obtains the exact covariance matrix $\boldsymbol{R}_{syn} = 1.44 \cdot 10^{-6} \cdot \boldsymbol{I}_2$ rad^2, related to the synthetic measurement vector $\boldsymbol{z}$. Within this setup, the assigned measurement noise covariance $\boldsymbol{R}^\star$ is intentionally chosen to be three times the value of the synthesized covariance $\boldsymbol{R}_{syn}$, resulting in $\boldsymbol{R}^\star = 4.32 \cdot 10^{-6} \cdot \boldsymbol{I}_2$ rad^2. The octarotor is required to maintain the initial hover condition at $t_0 = 0$ s with $\boldsymbol{p}(0) = [0,\, 0,\, -30]^T$ m, $\boldsymbol{v}(0) = [0,\, 0,\, 0]^T$ m/s, and $\boldsymbol{\eta}(0) = [0,\, 0,\, 0]$ rad, provided that $\xi_A(0) = \zeta_A(0)$ deg, $\dot{\xi}_A(0) = \dot{\xi}_B(0) = \dot{\zeta}_A(0) = \dot{\zeta}_B(0)$ deg/s, and $\xi_B(0) = \zeta_B(0) = 5$ deg. The set point position is thus a constant equal to $\boldsymbol{p}_{sp} = \boldsymbol{p}(0)$, the desired yaw angle is $\psi_{sp} = 0$ rad, and payload control is initially disabled, $\boldsymbol{a}^{(PC)}_{sp} = \boldsymbol{0}_{3\times1}$ m/s^2.

Figure 4 presents the results of a sample run with $\beta = 0.99$ in calm atmospheric conditions, illustrating the estimator's rapid convergence to a steady state. Specifically, the plot compares the true value, $x_2 = \zeta_B$, with its estimate, $\tilde{x}_2$, over a 60 s interval. During this time, the nominal covariance component $E_{2,2}$, and thus the estimator gain, settles at a constant value. A similar behavior is observed in the estimation of the angular rate $x_6 = \dot{\zeta}_B$, as shown in Figure 5. With respect to payload A, results are detailed in Figure 6, where satisfactory accuracy characterizes the estimation task in the presence of oscillations with a higher harmonic content. Similar results are obtained for the lateral oscillatory dynamics.

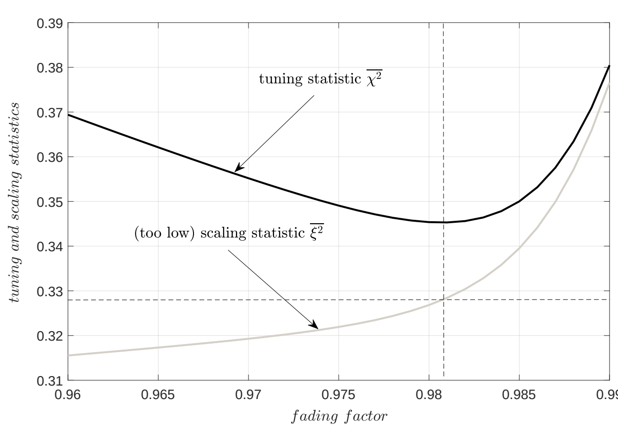

Figure 7: Analysis of the averaged tuning and scaling statistics over the filter bank (assigned $\boldsymbol{R}^\star$).

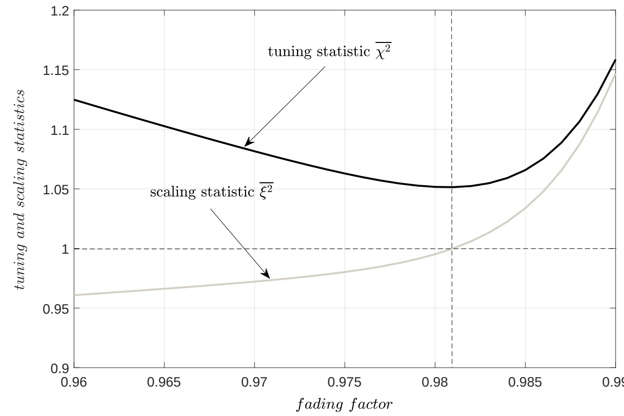

Figure 8: Analysis of the averaged tuning and scaling statistics over the filter bank (scaled $\boldsymbol{R}^\star$).

Figure 7 shows time–averaged results obtained in the estimator's steady state condition for simulations performed over 60 s. A range of β from 0.96 to 0.99, distributed over 31 filters, shows the effects predicted by theory. The tuning statistic $\overline{\chi^2}$ goes through a minimum on about the 22–nd filter, where $\beta = \beta_T = 0.981$. As a matter of fact, the value of the scaling statistic results to be too low, with $\overline{\xi^2}(\beta_T) = 0.3284 < 1$, meaning that the assigned $\boldsymbol{R}^\star$ is too high. At the best value $\beta = \beta_T$, the average scaling statistic $\overline{\xi^2}(\beta_T) = 0.3284$ is thus used to properly scale $\boldsymbol{R}^\star$ to an improved estimate of $\boldsymbol{R}_{syn}$, namely $\tilde{\boldsymbol{R}} = \overline{\xi^2}(\beta_T)\,\boldsymbol{R}^\star = 1.42{\cdot}10^{-6}{\cdot}\boldsymbol{I}_2$ rad$^2 \approx \boldsymbol{R}_{syn}$, according to the procedure described in Ref. 29. The current estimate $\tilde{\boldsymbol{R}}$, representing the expected value of the noise covariance matrix, is employed to recompute the filter bank across the same range of β (see Fig. 8). The tuning statistic continues to identify the same optimal filter, although the corresponding minimum value differs. Concurrently, the scaling statistic now crosses unity at the tuned condition, indicating that the newly assigned $\boldsymbol{R}^\star$ constitutes the best available estimate of $\boldsymbol{R}_{syn}$. As shown in Fig. 9, the trace of the true covariance $\boldsymbol{P}$, evaluated over the updated filter bank using $\boldsymbol{R}^\star$, attains its minimum near β_T, further validating the effectiveness of the tuning statistic in identifying the globally optimal filter. Additionally, the intersection between the true and the nominal error covariance curve as obtained through the trace operator, occurs close to this tuned condition at about $\beta_{P_{min}} = 0.978$ ($-0.36\,\%$ error with respect to β_T), showing that the nominal error covariance approximates the true covariance under the tuned and scaled configuration.

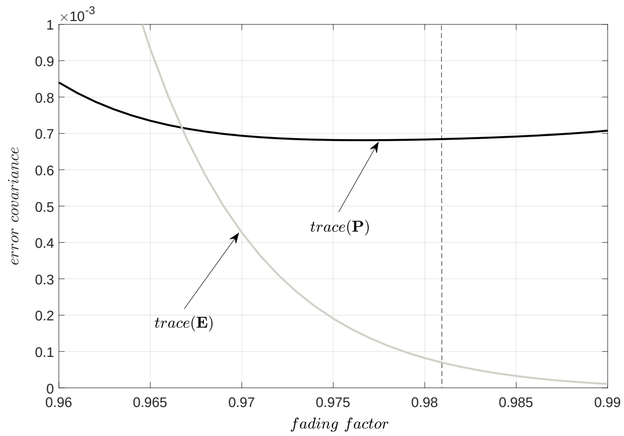

Figure 9: Analysis of the trace of nominal and true error covariance matrices over the filter bank (scaled $\boldsymbol{R}^{\star}$).

4.4. Delivery test case

The octarotor is initialized under the same conditions adopted for the tuning procedure, with the payloads at rest, and the filter is setup to deliver optimal performance ($\beta = \beta_T = 0.981$ and $\boldsymbol{R}^{\star} = 1.42 \cdot 10^{-6} \cdot \boldsymbol{I}_2$ rad^2) under the loading configuration discussed in Section 4.3. The vehicle is required to follow a sequence of prescribed waypoints $\mathbf{WP}_i = [x_i,\, y_i,\, z_i]^T$, $i = 1, \ldots, 5$, as listed in Table 2. Each waypoint is deemed to be reached when two conditions are simultaneously satisfied: (1) the positioning error, defined as $\varepsilon_P = \|\mathbf{WP}_i - \boldsymbol{p}\|$, falls below 0.3 m and (2) both cable oscillation angles $\varepsilon_A \geq 0$ and $\varepsilon_B \geq 0$ remain bounded under 3 deg for a continuous duration of 10 s. Cable oscillation angles ε_A and ε_B are respectively defined as the angles between the local vertical axis and each cable's direction, namely

$$\varepsilon_A = \arccos\left(\boldsymbol{z}_E \cdot \hat{\boldsymbol{c}}_A\right), \quad \varepsilon_B = \arccos\left(\boldsymbol{z}_E \cdot \hat{\boldsymbol{c}}_B\right) \tag{50}$$

Delivery tasks are performed according to the program detailed in the 5–th and 7–th column of Table 2, which define the expected payload conditions, denoted as m_{Ai} and m_{Bi}, when $\mathbf{WP}_i$ is designated as the setpoint. For instance, at $i = 1$, the octarotor departs from its initial position and moves toward $\mathbf{WP}_1$ carrying $m_{A1} = 60$ kg and $m_{B1} = 40$ kg. Upon arrival at $\mathbf{WP}_1$, load B is released, resulting in $m_{A2} = 60$ kg and $m_{B2} = 0$ kg, and the vehicle continues toward the next setpoint, $\mathbf{WP}_2$.

Table 2: List of waypoints.

WP	$[x_i,\, y_i,\, z_i]$ [m]	m_A [kg]	A_A [m^2]	m_B [kg]	A_B [m^2]
1	$[10,\, 0,\, -50]$	60	0.785	40	0.385
2	$[20,\, -10,\, -50]$	60	0.785	0	0
3	$[20,\, 10,\, -50]$	60	0.785	20	0.193
4	$[30,\, 0,\, -50]$	60	0.785	48	0.462
5	$[30,\, 10,\, -50]$	60	0.785	0	0

Certain waypoints, such as $\mathbf{WP}_2$ and $\mathbf{WP}_3$, serve as loading points where the value of m_B increases. In contrast, waypoints like $\mathbf{WP}_1$, $\mathbf{WP}_4$, and $\mathbf{WP}_5$, correspond to delivery locations where part of the payload is dropped. In the latter case, the closed–loop system reverts to the single payload scenario, such that $\boldsymbol{p}_C \equiv \boldsymbol{p}_A$, and continuity of operation characterizes the control strategy in Eq. (40), according to Remark 2. In such a case, one has:

$$\begin{aligned} \boldsymbol{p}_C - \boldsymbol{p}_H \approx L_A \big[&\sin\zeta_A, \quad -\sin\xi_A\, \cos\zeta_A, \\ &\cos\xi_A\, \cos\zeta_A\big]^T \end{aligned} \tag{51}$$

and

$$\begin{aligned} \boldsymbol{v}_C - \boldsymbol{v}_H \approx L_A \big[&\dot{\zeta}_A\, c\zeta_A, \quad -\dot{\xi}_A\, c\xi_A\, c\zeta_A \\ &+ \dot{\zeta}_A\, s\xi_A\, s\zeta_A, \\ &- \dot{\xi}_A\, s\xi_A\, c\zeta_A - \dot{\zeta}_A\, c\xi_A\, s\zeta_A\big]^T \end{aligned} \tag{52}$$

Accordingly, the estimation procedure switches to the method presented in Ref. 28, where the EKF is used to estimate the lateral ($\xi = \xi_A$) and the frontal ($\zeta = \zeta_A$) oscillation angle of the remaining payload through the same acceleration and attitude measurements of the FGDF. The two filters are thus executed in parallel, provided the EKF is initialized with $\tilde{\boldsymbol{x}}^{(0)-}\Big|_{EKF} = [\tilde{\xi}_A(0),\, \tilde{\zeta}_A(0),\, \dot{\tilde{\xi}}_A(0),\, \dot{\tilde{\zeta}}_A(0),\, \tilde{f}_{d1},\, \tilde{f}_{d2},\, \tilde{f}_{d3}]^T = \mathbf{0}_{7\times 1}$ and $\boldsymbol{E}^{(0)-}\Big|_{EKF} = \mathrm{diag}(10^{-6},\, 10^{-6},\, 10^{-6},\, 10^{-6},\, 1,\, 1,\, 10^{-5})$, the latter being the estimated covariance matrix. In this respect, the assigned noise covariance matrix is $\boldsymbol{R} = 2.25 \cdot 10^{-4} \cdot \boldsymbol{I}_3$ m^2/s^4 and process noise is accounted by $\boldsymbol{Q} = \mathrm{diag}(10^{-5},\, 10^{-5},\, 10^{-5},\, 10^{-5},\, 1,\, 1,\, 10^{-5})$, both matrices assumed to be constant. For the sake of brevity, the EKF tuning procedure to find the optimal configuration of $\boldsymbol{R}$ and $\boldsymbol{Q}$ is not detailed. It is noted that, while the EKF operates in the tuned condition during single–payload mission phases, the FGDF results to be suboptimal in loading configurations where $m_A \neq 40$ kg. The deliberate, albeit conservative, omission of the fading parameter adjustment is intended to assess filter performance in the presence of model uncertainties and errors.

During the mission, gusts are introduced to disturb the states of both the octarotor and the payloads. The turbulence is modeled using a dedicated Simulink Aerospace Blockset component, which implements the Von Kármán spectral representation. The approach is grounded in the mathematical formulations provided by the Military Specification MIL–F–8785C and the Military Handbook MIL–HDBK–1797B, referenced in Refs. 36 and 37, respectively. The following parameters are configured:

- specification: MIL–F–8785C;
- model type: continuous Von Kármán (+q +r);
- wind speed at 6 m (used to define the low–altitude wind intensity): 5 m/s;
- wind direction at 6 m (degrees clockwise from North): 90 deg;
- scale length at medium/high altitudes: 533.4 m (default value);
- MR wingspan: 2.38 m (here intended as the maximum octa–rotor frontal size);
- load wingspan: 1 m for load A, 0.7 m for load B (here intended as the maximum load frontal size);

while full modeling details are provided in Ref. 28. In addition to the considered turbulence contribution, a horizontal East wind with constant 10 m/s intensity is considered.

In Fig. 10 the trajectory followed by the octarotor is reported for the case when no active payload stabilization is performed, namely $\boldsymbol{a}_{sp}^{(PC)} = \mathbf{0}_{3\times1}$ m/s^2.

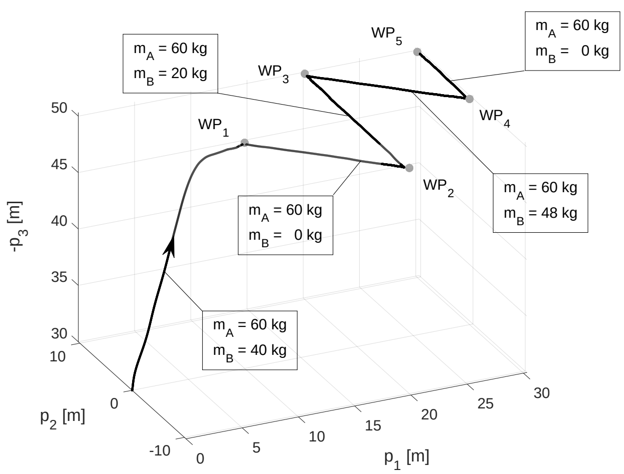

Figure 10: Trajectory followed by the octarotor based on a set of prescribed waypoints ($\boldsymbol{a}_{sp}^{(PC)} = \mathbf{0}_{3\times1}$ m/s^2).

Figure 11 presents a comparison between the true frontal oscillation variables of load A and their respective estimates obtained using the FGDF (solid gray line) and the EKF (dotted gray line). Correspondingly, Fig. 12 illustrates the same comparison for load B, restricted to the time intervals during which $m_B \neq 0$ kg. As expected, both estimation tasks exhibit satisfactory accuracy under nominal and near–nominal payload conditions. Reduced accuracy is observed during the mission phase between **WP**$_2$ and **WP**$_3$, where the knowledge of m_B is affected by a $-50\,\%$ uncertainty. Nonetheless, the FGDF continues to capture the macroscopic behavior, albeit with increased estimation noise.

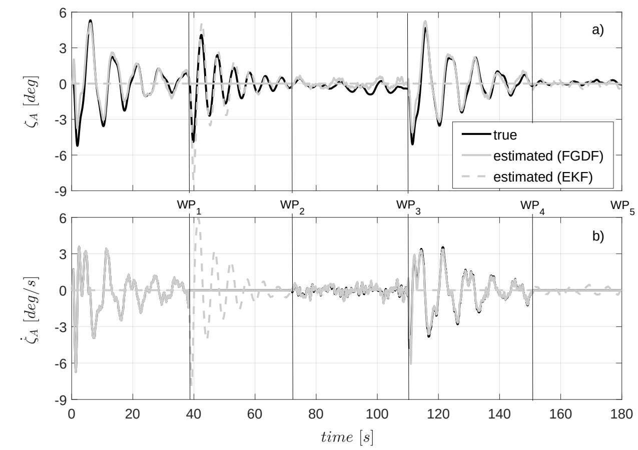

Figure 11: Comparison between the true and the estimated frontal oscillation states of load A. ($\boldsymbol{a}_{sp}^{(PC)} = \mathbf{0}_{3\times1}$ m/s^2).

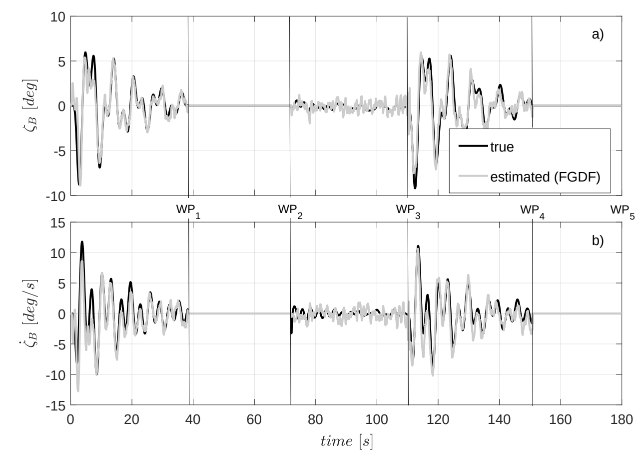

Figure 12: Comparison between the true and the estimated frontal oscillation states of load B. ($\boldsymbol{a}_{sp}^{(PC)} = \mathbf{0}_{3\times1}$ m/s^2).

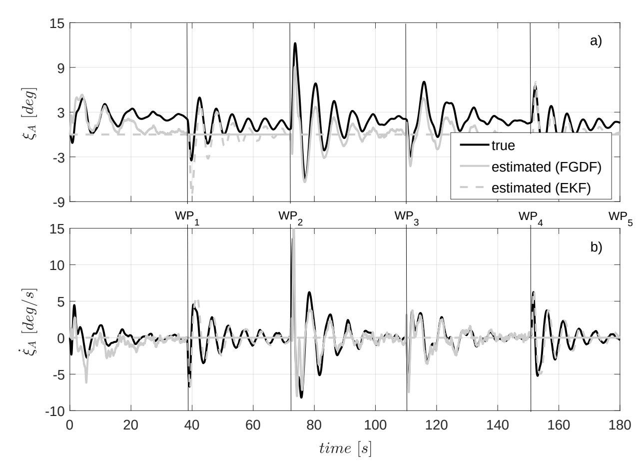

Figure 13: Comparison between the true and the estimated lateral oscillation states of load A. ($\boldsymbol{a}_{sp}^{(PC)} = \mathbf{0}_{3\times1}$ m/s^2).

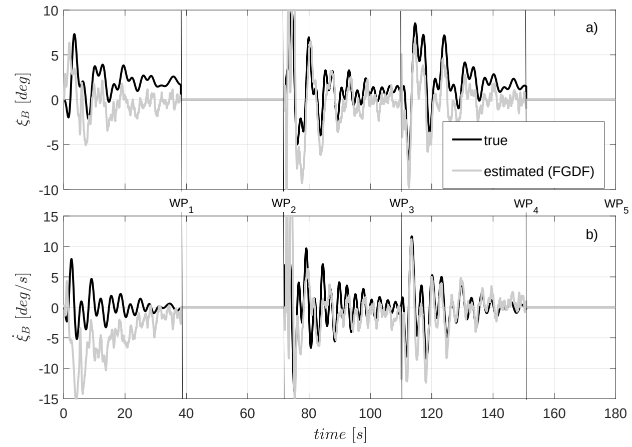

Figure 14: Comparison between the true and the estimated lateral oscillation states of load B. ($\boldsymbol{a}_{sp}^{(PC)} = \mathbf{0}_{3\times 1}$ m/s^2).

Figures 13 and 14 compare the true and estimated lateral oscillation states for loads A and B, respectively. A bias appears in the estimation of the oscillation angles ξ_A and ξ_B (leading to a maximum positioning error of approximately 0.7 m for the lower load), which is attributed to the influence of the constant East wind contribution. This wind induces a persistent lateral oscillation angle due to aerodynamic drag on the payloads, an effect that is not captured by the observation model described in Eq. (26). Specifically, under steady–state conditions where $a_2 = 0$ m/s^2 and $u_2 = 0$ N, the lateral angle measured by Eq. (26) is indeed zero. In addition, the nominal scenario in which both cables align with the local vertical no longer corresponds to a true equilibrium point. Hence, the eventual application of the auxiliary controller in Eq. (40) apparently becomes inconsistent with the system's actual dynamics, since the term $\mathrm{diag}(1,\,1,\,0)\ [k_p\,(\boldsymbol{p}_C - \boldsymbol{p}_H)]$ would provide a residual, steady–state contribution. In contrast, the term $\mathrm{diag}(1,\,1,\,0)\ [k_v\,(\boldsymbol{v}_C - \boldsymbol{v}_H)]$ would contribute with a significant damping effect, regardless of the filter's limitations, based on the accurate estimation of $\boldsymbol{v}_C - \boldsymbol{v}_H$. In what follows, the implementation of PC is discussed, while clarifying the effect of $\mathrm{diag}(1,\,1,\,0)\ [k_p\,(\boldsymbol{p}_C - \boldsymbol{p}_H)]$ from a practical standpoint.

In the case when PC is activated based on FGDF information, the mission is executed with performance indicators listed in the third column of Table 3, introduced to quantify the beneficial effects of the auxiliary controller. A comparison, summarized in the second column, is also provided with the case when $\boldsymbol{a}_{sp}^{(PC)} = \mathbf{0}_{3\times 1}$ m/s^2.

Table 3: Summary of performance indices.

index	no PC	PC (FGDF+EKF)
t_m [s]	180.7	177.4 (-1.8 %)
E_{prop} [Wh]	1 161.0	1 140.2 (-1.8 %)
$\bar{\varepsilon}_A$ [deg]	2.52	2.15 (-14.7 %)
$\bar{\varepsilon}_B$ [deg]	2.03	1.69 (-16.7 %)
$\bar{\nu}_A$ [deg/s]	2.05	1.68 (-18.0 %)
$\bar{\nu}_B$ [deg/s]	3.17	2.23 (-29.7 %)
$\bar{a}_A$ [m/s^2]	0.39	0.27 (-30.8 %)
$\bar{a}_B$ [m/s^2]	2.22	1.71 (-23.0 %)

For the aim of the present analysis, let t_m be the total time required to perform the maneuver and reach the final waypoint. Average swing angles are defined as $\bar{\varepsilon}_A = I_{\varepsilon A}(t_m)/t_m$ and $\bar{\varepsilon}_B = I_{\varepsilon B}(t_m)/t_m$, where the integrals

$$(53)\quad I_{\varepsilon A}(t_m) = \int_0^{t_m} |\varepsilon_A(s)|\, ds$$

and

$$(54)\quad I_{\varepsilon B}(t_m) = \int_0^{t_m} |\varepsilon_B(s)|\, ds$$

are evaluated over t_m. Similarly, average swing rates $\bar{\nu}_A$ and $\bar{\nu}_B$ are introduced. Let $\nu_A = \dot{\varepsilon}_A$ and $\nu_B = \dot{\varepsilon}_B$ be the time derivatives of $\varepsilon_A(t)$ and $\varepsilon_B(t)$, respectively. Then, $\bar{\nu}_A$ and $\bar{\nu}_B$ are calculated through the integrals

$$(55)\quad \bar{\nu}_A = \sqrt{\frac{1}{t_m}\int_0^{t_m} \nu_A^2(s)\, ds}$$

and

$$(56)\quad \bar{\nu}_B = \sqrt{\frac{1}{t_m}\int_0^{t_m} \nu_B^2(s)\, ds}$$

E_{prop} is the mechanical energy delivered by electrical motors to propellers, calculated by the integral

$$(57)\quad E_{prop} = \int_0^{t_m} \sum_{j=1}^{8} P_{sh\,j}(s)\, ds$$

and expressed in Wh, where $P_{sh\,j} = Q_j\,\Omega_j$ is the output shaft power generated by the j–th motor, $j = 1, \ldots, 8$, obtained from required torque Q_j and angular rate Ω_j, under the assumption of null friction torque. Finally, the amplitudes of the accelerations of the two payloads are given, provided $\boldsymbol{a}_A = \dot{\boldsymbol{v}}_A$ and $\boldsymbol{a}_B = \dot{\boldsymbol{v}}_B$. Average values are respectively obtained as

$$(58)\quad \bar{a}_A = \frac{1}{t_m}\int_0^{t_m} \|\boldsymbol{a}_A(s)\|\, ds$$

and

$$(59)\quad \bar{a}_B = \frac{1}{t_m}\int_0^{t_m} \|\boldsymbol{a}_B(s)\|\, ds$$

Table 3 shows that the estimation strategy, combined with the proposed payload control method, enables the system to complete the same mission in approximately the same maneuver time and with comparable battery consumption. Notably, the swing motion of both payloads is significantly reduced. This is particularly evident in the average swing angles, which decrease by approximately $14.7\,\%$ for the upper load and $16.7\,\%$ for the lower load. Similar considerations hold for the average swing rates, with diminutions amounting respectively to $18\,\%$ and $29.7\,\%$. Even more promising are the acceleration results, with amplitude reductions of about $30.8\,\%$ and $23\,\%$, respectively, which represents a critical objective when ensuring the payload is protected from undesired mechanical stress is of paramount importance. Although initial concerns were raised, it is observed that the proportional term $\mathrm{diag}(1,\,1,\,0)\,[k_p\,(\boldsymbol{p}_C-\boldsymbol{p}_H)]$ proves effective in attenuating oscillation angles during phases of accelerated motion. Nonetheless, it provides no contribution under steady–state conditions, where residual angular deviations inherently persist in the physical system but remain unperceived by the filter and, consequently, by the controller. In this context, the inherent limitations of the filter actually translate into a beneficial reduction of control activity.

5. Conclusions

This work introduces a robust estimation algorithm tailored for managing the swing dynamics of dual payloads suspended from a multirotor aerial platform, with specific applicability to urban air mobility scenarios. The method employs a recursive Fading Gaussian Deterministic Filter, which fuses onboard acceleration data with predictive dynamic modeling in a linearized framework. The system is modeled as a three–point–mass configuration interconnected by rigid, massless cables, capturing essential dynamics without excessive computational burden.

High–fidelity numerical simulations confirm the effectiveness of the approach in environments reflective of real–world UAM operations, including the nonlinear behavior of an octarotor platform, elastic cable effects, system uncertainties, and external disturbances. To support practical deployment, a tuning methodology is proposed to identify the optimal filter settings that trade off model uncertainty and sensor noise. The filter's inherent ability to infer and counteract external disturbances makes it well suited for integration into real–time feedback control systems. This is demonstrated in a mission–relevant scenario where an octarotor executes a complex waypoint–following task, representing a simple parcel delivery, under varying operational conditions. The filter and control strategy are evaluated in terms of their capacity to minimize payload oscillations and maintain dynamic loads within thresholds that preserve payload integrity, offering a compelling solution for next–generation aerial logistics in urban environments or industrial plants.

Appendix A: Elements of matrices $\boldsymbol{M}$ and $\boldsymbol{C}$

In what follows, non–null elements of $\boldsymbol{M}\in\mathbb{R}^{7\times7}$ and $\boldsymbol{C}\in\mathbb{R}^{7\times7}$ in Eq. (10) are reported.

$$M_{1,1}=m+m_A+m_B=M_{2,2}=M_{3,3} \tag{60}$$

$$M_{1,5}=L_B\,m_B\,\cos\zeta_B=M_{5,1} \tag{61}$$

$$M_{1,7}=L_A\,(m_A+m_B)\,\cos\zeta_A=M_{7,1} \tag{62}$$

$$M_{2,4}=-L_B\,m_B\,\cos\xi_B\,\cos\zeta_B=M_{4,2} \tag{63}$$

$$M_{2,5}=L_B\,m_B\,\sin\xi_B\,\sin\zeta_B=M_{5,2} \tag{64}$$

$$M_{2,6}=-L_A\,(m_A+m_B)\,\cos\xi_A\,\cos\zeta_A=M_{6,2} \tag{65}$$

$$M_{2,7}=L_A\,(m_A+m_B)\,\sin\xi_A\,\sin\zeta_A=M_{7,2} \tag{66}$$

$$M_{3,4}=-L_B\,m_B\,\sin\xi_B\,\cos\zeta_B=M_{4,3} \tag{67}$$

$$M_{3,5}=-L_B\,m_B\,\cos\xi_B\,\sin\zeta_B=M_{5,3} \tag{68}$$

$$M_{3,6}=-L_A\,(m_A+m_B)\,\sin\xi_A\,\cos\zeta_A=M_{6,3} \tag{69}$$

$$M_{3,7}=-L_A\,(m_A+m_B)\,\cos\xi_A\,\sin\zeta_A=M_{7,3} \tag{70}$$

$$M_{4,4}=L_B^2\,m_B\,\cos^2\zeta_B \tag{71}$$

$$\begin{aligned}M_{4,6}=L_A\,L_B\,m_B\,(&\cos\xi_A\,\cos\zeta_A\,\cos\xi_B\,\cos\zeta_B\\&+\sin\xi_A\,\cos\zeta_A\,\sin\xi_B\,\cos\zeta_B)=M_{6,4}\end{aligned} \tag{72}$$

$$\begin{aligned}M_{4,7}=L_A\,L_B\,m_B\,(&-\sin\xi_A\,\sin\zeta_A\,\cos\xi_B\,\cos\zeta_B\\&+\cos\xi_A\,\sin\zeta_A\,\sin\xi_B\,\cos\zeta_B)=M_{7,4}\end{aligned} \tag{73}$$

$$M_{5,5}=L_B^2\,m_B \tag{74}$$

$$\begin{aligned}M_{5,6}=L_A\,L_B\,m_B\,(&-\cos\xi_A\,\cos\zeta_A\,\sin\xi_B\,\sin\zeta_B\\&+\sin\xi_A\,\cos\zeta_A\,\cos\xi_B\,\sin\zeta_B)=M_{6,5}\end{aligned} \tag{75}$$

$$\begin{aligned}M_{5,7}=L_A\,L_B\,m_B\,(&\sin\xi_A\,\sin\zeta_A\,\sin\xi_B\,\sin\zeta_B\\&+\cos\xi_A\,\sin\zeta_A\,\cos\xi_B\,\sin\zeta_B\\&+\cos\xi_A\,\cos\zeta_A)=M_{7,5}\end{aligned} \tag{76}$$

$$M_{6,6}=L_A^2\,(m_A+m_B)\cos^2\zeta_A \tag{77}$$

$$M_{7,7}=L_A^2\,(m_A+m_B) \tag{78}$$

$$C_{1,5}=-L_B\,m_B\,\dot{\zeta}_B\,\sin\zeta_B \tag{79}$$

$$C_{1,7}=-L_A\,(m_A+m_B)\,\dot{\zeta}_A\,\sin\zeta_A \tag{80}$$

$$\begin{aligned}C_{2,4}=L_B\,m_B\,(&\dot{\xi}_B\,\sin\xi_B\,\cos\zeta_B\\&+\dot{\zeta}_B\,\cos\xi_B\,\sin\zeta_B)\end{aligned} \tag{81}$$

$$C_{2,5} = L_B\, m_B\, (\dot\xi_B\, \cos\xi_B\, \sin\zeta_B + \dot\zeta_B\, \sin\xi_B\, \cos\zeta_B) \tag{82}$$

$$C_{2,6} = L_A\, (m_A + m_B)\, (\dot\xi_A\, \sin\xi_A\, \cos\zeta_A + \dot\zeta_A\, \cos\xi_A\, \sin\zeta_A) \tag{83}$$

$$C_{2,7} = L_A\, (m_A + m_B)\, (\dot\xi_A\, \cos\xi_A\, \sin\zeta_A + \dot\zeta_A\, \sin\xi_A\, \cos\zeta_A) \tag{84}$$

$$C_{3,4} = -L_B\, m_B\, (\dot\xi_B\, \cos\xi_B\, \cos\zeta_B - \dot\zeta_B\, \sin\xi_B\, \sin\zeta_B) \tag{85}$$

$$C_{3,5} = L_B\, m_B\, (\dot\xi_B\, \sin\xi_B\, \sin\zeta_B - \dot\zeta_B\, \cos\xi_B\, \cos\zeta_B) \tag{86}$$

$$C_{3,6} = L_A\, (m_A + m_B)\, (-\dot\xi_A\, \cos\xi_A\, \cos\zeta_A + \dot\zeta_A\, \sin\xi_A\, \sin\zeta_A) \tag{87}$$

$$C_{3,7} = L_A\, (m_A + m_B)\, (\dot\xi_A\, \sin\xi_A\, \sin\zeta_A - \dot\zeta_A\, \cos\xi_A\, \cos\zeta_A) \tag{88}$$

$$C_{4,4} = -L_B^2\, m_B\, \dot\zeta_B\, \sin\zeta_B\, \cos\zeta_B \tag{89}$$

$$C_{4,5} = -L_B^2\, m_B\, \dot\xi_B\, \sin\zeta_B\, \cos\zeta_B \tag{90}$$

$$\begin{aligned} C_{4,6} = {} & L_A\, L_B\, m_B\, \dot\xi_A\, (-\sin\xi_A\, \cos\zeta_A\, \cos\xi_B\, \cos\zeta_B + \cos\xi_A\, \cos\zeta_A\, \sin\xi_B\, \cos\zeta_B) \\ & - L_A\, L_B\, m_B\, \dot\zeta_A\, (\cos\xi_A\, \sin\zeta_A\, \cos\xi_B\, \cos\zeta_B + \sin\xi_A\, \sin\zeta_A\, \sin\xi_B\, \cos\zeta_B) \end{aligned} \tag{91}$$

$$\begin{aligned} C_{4,7} = {} & -L_A\, L_B\, m_B\, \dot\xi_A\, (\cos\xi_A\, \sin\zeta_A\, \cos\xi_B\, \cos\zeta_B + \sin\xi_A\, \sin\zeta_A\, \sin\xi_B\, \cos\zeta_B) \\ & + L_A\, L_B\, m_B\, \dot\zeta_A\, (\cos\xi_A\, \cos\zeta_A\, \sin\xi_B\, \cos\zeta_B - \sin\xi_A\, \cos\zeta_A\, \cos\xi_B\, \cos\zeta_B) \end{aligned} \tag{92}$$

$$C_{5,4} = L_B^2\, m_B\, \dot\xi_B\, \sin\zeta_B\, \cos\zeta_B \tag{93}$$

$$\begin{aligned} C_{5,6} = {} & L_A\, L_B\, m_B\, \dot\xi_A\, (\sin\xi_A\, \cos\zeta_A\, \sin\xi_B\, \sin\zeta_B + \cos\xi_A\, \cos\zeta_A\, \cos\xi_B\, \sin\zeta_B) \\ & + L_A\, L_B\, m_B\, \dot\zeta_A\, (\cos\xi_A\, \sin\zeta_A\, \sin\xi_B\, \sin\zeta_B - \sin\xi_A\, \sin\zeta_A\, \cos\xi_B\, \sin\zeta_B) \end{aligned} \tag{94}$$

$$\begin{aligned} C_{5,7} = {} & L_A\, L_B\, m_B\, \dot\xi_A\, (\cos\xi_A\, \sin\zeta_A\, \sin\xi_B\, \sin\zeta_B - \sin\xi_A\, \sin\zeta_A\, \cos\xi_B\, \sin\zeta_B) \\ & + L_A\, L_B\, m_B\, \dot\zeta_A\, (\sin\xi_A\, \cos\zeta_A\, \sin\xi_B\, \sin\zeta_B + \cos\xi_A\, \cos\zeta_A\, \cos\xi_B\, \sin\zeta_B - \sin\zeta_A\, \cos\zeta_B) \end{aligned} \tag{95}$$

$$\begin{aligned} C_{6,4} = {} & L_A\, L_B\, m_B\, \dot\xi_B\, (-\cos\xi_A\, \cos\zeta_A\, \sin\xi_B\, \cos\zeta_B + \sin\xi_A\, \cos\zeta_A\, \cos\xi_B\, \cos\zeta_B) \\ & - L_A\, L_B\, m_B\, \dot\zeta_B\, (\cos\xi_A\, \cos\zeta_A\, \cos\xi_B\, \sin\zeta_B + \sin\xi_A\, \cos\zeta_A\, \sin\xi_B\, \sin\zeta_B) \end{aligned} \tag{96}$$

$$\begin{aligned} C_{6,5} = {} & -L_A\, L_B\, m_B\, \dot\xi_B\, (\cos\xi_A\, \cos\zeta_A\, \cos\xi_B\, \sin\zeta_B + \sin\xi_A\, \cos\zeta_A\, \sin\xi_B\, \sin\zeta_B) \\ & + L_A\, L_B\, m_B\, \dot\zeta_B\, (\sin\xi_A\, \cos\zeta_A\, \cos\xi_B\, \cos\zeta_B - \cos\xi_A\, \cos\zeta_A\, \sin\xi_B\, \cos\zeta_B) \end{aligned} \tag{97}$$

$$\begin{aligned} C_{7,4} = {} & L_A\, L_B\, m_B\, \dot\xi_B\, (\sin\xi_A\, \sin\zeta_A\, \sin\xi_B\, \cos\zeta_B + \cos\xi_A\, \sin\zeta_A\, \cos\xi_B\, \cos\zeta_B) \\ & + L_A\, L_B\, m_B\, \dot\zeta_B\, (\sin\xi_A\, \sin\zeta_A\, \cos\xi_B\, \sin\zeta_B - \cos\xi_A\, \sin\zeta_A\, \sin\xi_B\, \sin\zeta_B) \end{aligned} \tag{98}$$

$$\begin{aligned} C_{7,5} = {} & L_A\, L_B\, m_B\, \dot\xi_B\, (\sin\xi_A\, \sin\zeta_A\, \cos\xi_B\, \sin\zeta_B - \cos\xi_A\, \sin\zeta_A\, \sin\xi_B\, \sin\zeta_B) \\ & + L_A\, L_B\, m_B\, \dot\zeta_B\, (\sin\xi_A\, \sin\zeta_A\, \sin\xi_B\, \cos\zeta_B + \cos\xi_A\, \sin\zeta_A\, \cos\xi_B\, \cos\zeta_B - \cos\zeta_A\, \sin\zeta_B) \end{aligned} \tag{99}$$

Acknowledgments

This study was carried out within the MOST - Sustainable Mobility National Research Center and received funding from the European Union Next-GenerationEU (PIANO NAZIONALE DI RIPRESA E RESILIENZA (PNRR) - MISSIONE 4 COMPONENTE 2, INVESTIMENTO 1.4 - D.D. 1033 17/06/2022, CN00000023). This manuscript reflects only the authors' views and opinions, neither the European Union nor the European Commission can be considered responsible for them.

References

[1] Estevez, J., Garate, G., Lopez-Guede, J.M., Larrea, M., Review of Aerial Transportation of Suspended-Cable Payloads with Quadrotors, Drones 8(35) (2024) 35, https://doi.org/10.3390/drones8020035

[2] Pavel, M.D., Understanding the control characteristics of electric vertical take-off and landing (eVTOL) aircraft for urban air mobility, Aerosp. Sci. Technol. 125 (2022) 107143, https://doi.org/10.1016/j.ast.2021.107143

[3] Godbole, A.R., Subbarao, K., Nonlinear control of unmanned aerial vehicles with cable suspended payloads. Aerosp. Sci. Technol. 93 (2019) 105299, https://doi.org/10.1016/j.ast.2019.07.032

[4] Yi, J., Zhang, H., Wang, F., Ning, C., Liu, H., Zhong, G., An Operational Capacity Assessment Method for an Urban Low-Altitude Unmanned Aerial Vehicle Logistics Route Network, Drones 7(9) (2023) 582, https://doi.org/10.3390/drones7090582

[5] Chen, T., Shan, J., A novel cable-suspended quadrotor transportation system: From theory to experiment. Aerosp. Sci. Technol. 104 (2020) 105974, https://doi.org/10.1016/j.ast.2020.105974

[6] Palunko, I., Fierro, R., Cruz, P., Trajectory generation for swing-free maneuvers of a quadrotor with suspended payload: A dynamic programming approach, in: Proc. of the 2012 IEEE International Conference on Robotics and Automation (ICRA), Saint Paul, MN, USA, 2012, pp. 2691-269, https://doi.org/10.1109/ICRA.2012.6225213

[7] de Angelis, E.L., Giulietti, F., Pipeleers, G., Two-time-scale control of a multirotor aircraft for suspended load transportation, Aerosp. Sci. Technol. 84 (2019) 193-203, https://doi.org/10.1016/j.ast.2018.10.012

[8] Nicotra, M.M., Garone, E., Naldi, R., Marconi, L., in: Proc. of the 2014 American Control Conference, Portland, OR, USA, 2014, pp. 3585-3590, https://doi.org/10.1109/ACC.2014.6859222

[9] Guerrero, M., Mercado, D., Lozano, R., García, C., Passivity based control for a quadrotor UAV transporting a cable-suspended payload with minimum swing, in: Proc. of the 2015 IEEE Conference on Decision and Control (CDC), Osaka, Japan, 2015, pp. 6718-6723, https://doi.org/10.1109/CDC.2015.7403277

[10] Zhou, X., Liu, R., Zhang, J., Zhang, X., Stabilization of a quadrotor with uncertain suspended load using sliding mode control, in: Proc. of the International Design Engineering Technical Conferences and Computers and Information in Engineering Conference, Charlotte, NC, USA, 2016; 50152, American Society of Mechanical Engineers, New York, NY, USA, 2016, https://doi.org/10.1115/DETC2016-60060

[11] Yi, K., Liang, X., He, Y., Yang, L., Han, J., Active-model-based control for the quadrotor carrying a changed slung load, Electronics 8(4) (2019) 461, https://doi.org/10.3390/electronics8040461

[12] Yu, G., Xie, W., Cabecinhas, D., Cunha, R., Silvestre, C., Adaptive control with unknown mass estimation for a quadrotor-slung-load system, ISA Trans. 133 (2023) 412-423, https://doi.org/10.1016/j.isatra.2022.06.036

[13] Liang, X., Fang, Y., Sun, N., Lin, H., Dynamics analysis and time-optimal motion planning for unmanned quadrotor transportation systems, Mechatronics 50 (2018), 50, 16-29, https://doi.org/10.1016/j.mechatronics.2018.01.009

[14] Huo, X., Chen, J., Liu, Q., He, X., Vibration elimination for quadrotor slung system based on input shaping and double closed-loop control, in: Proc. of the Asian Control Conference (ASCC), Kitakyushu, Japan, June 2019, pp. 492-497.

[15] Kusznir, T., Smoczek, J., Sliding mode-based control of a UAV quadrotor for suppressing the cable-suspended payload vibration, J. Control Sci. Eng. 2020 (2020) 5058039, https://doi.org/10.1155/2020/5058039

[16] Slabber, J., Jordaan, H.W., Vision-Based Control of an Unknown Suspended Payload with a Multirotor, in: Proc. of the IEEE/RSJ International Conference on Intelligent Robots and Systems (IROS), Prague, Czech Republic, 2021, pp. 4875-4880, https://doi.org/10.1109/IROS51168.2021.9636648

[17] Wang, T., Zhou, J., Wu, Z., Liu, R., Zhang, J., Liang, Y., A Time-Varying PD Sliding Mode Control Method for the Container Crane Based on a Radial-Spring Damper, Electronics 11 (2022) 3543, https://doi.org/10.3390/electronics11213543

[18] How, J.P., Behihke, B., Frank, A., Dale, D., Vian, J., Realtime indoor autonomous vehicle test environment, IEEE Control Syst. 28(2) (2008) 51-64, https://doi.org/10.1109/MCS.2007.914691

[19] Lupashin, S., Hehn, M., Mueller, M.W., Schoellig, A.P., Sherback, M., D'Andrea, R., A platform for aerial robotics research and demonstration: the flying machine arena, Mechatronics 24(1) (2014) 41-54, https://doi.org/10.1016/j.mechatronics.2013.11.006

[20] Zürn, M., Morton, K., Heckmann, A., McFadyen, A., Notter, S., Gonzalez, F., MPC controlled multirotor with suspended slung load: system architecture and visual load detection, in: Proc. of IEEE Aerospace Conference 2016, pp. 1-11, https://doi.org/10.1109/AERO.2016.7500543

[21] Ebrahimi, M., Ghayour, M., Madani, S.M., Khoobroo, A., Swing angle estimation for anti-sway overhead crane control using load cell, Int. J. Control Autom. Syst. 9 (2011) 301-309, https://doi.org/10.1007/s12555-011-0212-5

[22] Feng, Y., Wang, J., GPS RTK Performance Characteristics and Analysis, J. Glob. Position. Syst. 7(1) (2008) 1-8, https://doi.org/10.5081/jgps.7.1.1

[23] Kim, Y.S., Hong, K.S., Sul, S.K., Anti-Sway Control of Container Cranes: Inclinometer, Observer, and State Feedback, Int. J. Control Autom. Syst. 2(4) (2004) 435-449, https://doi.org/10.1.1.454.9911

[24] Paul, H., Ono, K., Ladig, R., Shimonomura, K., A Multirotor Platform Employing a Three-Axis Vertical Articulated Robotic Arm for Aerial Manipulation Tasks, in: Proc. of IEEE/ASME International Conference on Advanced Intelligent Mechatronics (AIM), 2018, pp. 478-485, https://doi.org/10.1109/AIM.2018.8452699

[25] Lee, S.J., Kim, H.J., Autonomous Swing-Angle Estimation for Stable Slung-Load Flight of Multi-Rotor UAVs, in: Proc. of IEEE International Conference on Robotics and Automation (ICRA), 2017, pp. 4576-4581, https://doi.org/10.1109/ICRA.2017.7989532

[26] Lee, S., Son, H., Antisway Control of a Multirotor With Cable-Suspended Payload, IEEE Trans. Control Syst. Technol. 29(6) (2021) 2630-2638, https://doi.org/10.1109/TCST.2020.3035004

[27] de Angelis, E.L., Swing angle estimation for multicopter slung load applications, Aerosp. Sci. Technol. 89 (2019) 264-274, https://doi.org/10.1016/j.ast.2019.04.014

[28] de Angelis, E.L., Giulietti, F., An Improved Method for Swing State Estimation in Multirotor Slung Load Applications, Drones 7(11) (2023) 654, https://doi.org/10.3390/drones7110654

[29] de Angelis, E.L., Ferrarese, G., Giulietti, F., Modenini, D., Tortora, P., Terminal height estimation using a Fading Gaussian Deterministic filter, Aerosp. Sci. Technol. 55 (2016) 366-376, https://doi.org/10.1016/j.ast.2016.06.013

[30] PX4 Development Team and Community, PX4 Autopilot User Guide (main), <https://docs.px4.io/main/en/> (accessed 06/06/2025)

[31] de Ruiter, A.H.J., Damaren, C.J., Forbes, J.R., Spacecraft Dynamics and Control - An Introduction, John Wiley & Sons, Ltd., Sussex, 2013, pp. 19–24.

[32] Butcher, J.C., Numerical methods for ordinary differential equations in the 20th century, J. Comput. Appl. Math. 125 (2000) 1-29, https://doi.org/10.1016/S0377-0427(00)00455-6

[33] U.S. Government Printing Office, U.S. Standard Atmosphere 1976, NOAA–S/T 76–1562, pp. 1-241.

[34] Ogawa, S., Robust PID Controller Tuning for Input Disturbance Rejection, IFAC Proceedings Volumes 30(9) (1997) 295-300, https://doi.org/10.1016/S1474-6670(17)43171-5

[35] Higham, N.J., The Scaling and Squaring Method for the Matrix Exponential Revisited, SIAM J. Matrix Anal. Appl. 26(4) (2005) 1179-1193, https://doi.org/10.1137/04061101X

[36] U.S. Department of Defense, Flying Qualities of Piloted Airplanes, U.S. Military Specification MIL–F–8785C, 1980, pp. 1–95.

[37] U.S. Department of Defense, Flying Qualities of Piloted Aircraft, U.S. Military Handbook MIL–HDBK–1797B, 2012, pp. 1–849.